Characterizing Average Seasonal, Synoptic, and Finer Variability in Orbiting Carbon Observatory-2 XCO₂ across North America and Adjacent Ocean Basins

Enter authors here: Kayla A. Mitchell[1], Scott C. Doney[1], and Gretchen Keppel-Aleks[2]

[1]Environmental Sciences, University of Virginia, Charlottesville, VA, USA. [1]Environmental Sciences, University of Virginia, Charlottesville, VA, USA. [2]Climate and Space Sciences and Engineering, University of Michigan, Ann Arbor, MI, USA.

Corresponding author: K. A. Mitchell (kam9rc@virginia.edu)

†Additional author notes should be indicated with symbols (current addresses, for example).

Key Points:

- We attribute variability in XCO₂ retrieved from NASA's OCO-2 satellite to surface flux gradients, atmospheric transport, and error.

- Seasonal and synoptic-scale XCO₂ variability reflects hemispheric and continental-scale surface carbon flux gradients.

- Correlated errors impart spatially coherent fine-scale variability that significantly increases standard error in XCO₂ aggregates.

Abstract

Variations in atmosphere total column-mean CO_2 (XCO_2) collected by the National Aeronautics and Space Administration's Orbiting Carbon Observatory-2 satellite can be used to constrain surface carbon fluxes if the influence of atmospheric transport and observation errors on the data is known and accounted for. Due to sparse validation data, the portions of fine-scale variability in XCO_2 driven by fluxes, transport, or retrieval errors remains uncertain, particularly over the ocean. To better understand these drivers, we characterize variability in OCO-2 Level 2 version 10 XCO_2 from the seasonal scale, synoptic-scale (order of days, 1000s of kms), and mesoscale (within-day, 100s kms) for ten biomes over North America and adjacent ocean basins. Seasonal and synoptic variations in XCO_2 reflect real geophysical drivers (transport and fluxes), following large-scale atmospheric circulation and the north-south distribution of biosphere carbon uptake. In contrast, geostatistical analysis of mesoscale and finer variability shows that real signals are obscured by systematic biases across the domain. Spatial correlations in along-track XCO_2 are much shorter and spatially-coherent variability is much larger in magnitude than can be attributed to fluxes or transport. We characterize random and coherent along-track XCO_2 variability in addition to quantifying uncertainty in XCO_2 aggregates across typical lengths used in inverse modeling. Even over the ocean, correlated errors decrease the independence and increase uncertainty in XCO_2. We discuss the utility of computing geostatistical parameters and demonstrate their importance for XCO_2 science applications spanning from data reprocessing and algorithm development to error estimation and carbon flux inference.

Plain Language Summary

The National Aeronautics and Space Administration's Orbiting Carbon Observatory-2 satellite collects measurements of atmosphere total column-mean CO_2 (XCO_2), providing a constraint on surface carbon fluxes. Fluxes of carbon into Earth's surface by the ocean and land biosphere (uptake) counteract the rising levels of atmospheric CO_2 caused by increased anthropogenic emissions. To use XCO_2 for flux estimation in inverse models, variability in the data must be attributed to either gradients in surface carbon fluxes, atmospheric transport, or retrieval errors. We decompose OCO-2 XCO_2 variability over North America and adjacent ocean into seasonal, synoptic (order of days, 1000s of km) and finer scales to uncover the relative influences of these processes on XCO_2. Spatial patterns in seasonal and synoptic-scale XCO_2 variability follow large-scale atmospheric circulation and reflect the mean north-south distribution of biosphere carbon uptake in the Northern Hemisphere rather than underlying local surface flux variability. On finer scales, geostatistical analysis shows that patterns in XCO_2 variability are driven by correlated retrieval errors, obscuring the influence of transport and error. We compute new estimates of XCO_2 uncertainty for inverse model studies that assimilate the data and discuss the impact of errors over different land and ocean regions.

1 Introduction

Carbon flux accounting forms the basis of climate-science applications that guide policy, track fossil fuel emissions, monitor the biosphere, and project global change. Spatiotemporal variations in atmospheric carbon dioxide, CO_2, reflect the underlying uptake and release of CO_2 by surface processes and atmospheric transport. Consequently, atmospheric CO_2 measurements can provide a top-down constraint for carbon flux inference, given that the signal from surface fluxes is disentangled from transport-induced variability. Top-down flux inference, achieved through atmospheric inverse modeling, requires a quantitative description of transport-induced

variability and error in CO_2 measurements across a wide range of spatial and temporal scales. While there is currently good confidence in surface carbon fluxes estimated from inversion studies on hemispheric and annual scales, there is still disagreement in the corresponding surface fluxes on sub-annual and regional scales (Peiro et al., 2022; Gaubert et al., 2019; Baker et al., 2006; Gurney et al., 2002). Uncertainties arise due to the limited spatiotemporal coverage of observations, differing model representations of atmospheric transport and mixing, and poorly constrained regional surface flux heterogeneity. In the past decade, space-based instruments such as the National Aeronautics and Space Administration's Orbiting Carbon Observatory-2 (NASA OCO-2) satellite have provided a more complete global picture of total column average atmospheric CO_2, XCO_2 (Eldering et al., 2017).

Since its launch in July 2014, OCO-2 has measured XCO_2 with a high level of precision (between 0.1–0.5% or ~1 ppm error per individual sounding) (O'Dell et al., 2018; Wunch et al., 2017) capable of reducing uncertainties in regional carbon flux inference (Rayner and O'Brien, 2001; Miller et al., 2007). Because XCO_2 captures the CO_2 abundance throughout a total atmospheric column, including the planetary boundary layer and free troposphere, it is less sensitive to vertical mixing and entrainment than measurements made near the surface. This mediates the uncertainties in transport models that arise when representing small-scale vertical mixing and ties XCO_2 more directly to surface fluxes via mass balance (Basu et al., 2018; Olsen & Randerson, 2004; Rayner & O'Brien, 2001). However, XCO_2 is sensitive to rapid horizontal transport in the free troposphere, giving these measurements a large footprint that reflects large-scale flux patterns more than local processes (Keppel-Aleks et al., 2011). Atmospheric inversions of XCO_2 can thus constrain surface fluxes at regional and continental spatial scales,

bridging the gap between small-scale direct flux measurements, which must be extrapolated to other areas, and global constraints, which cannot capture regional dynamics.

Transport-induced XCO_2 variability arising from the mixing of XCO_2 concentration gradients must be resolved in inverse model frameworks to reveal surface flux information. The influence of transport on XCO_2 variability has been well-documented in time-series such as that from the Total Carbon Column Observing Network (TCCON) (Wunch et al., 2011). TCCON is a network of ground-based spectrometers with coverage that is more temporally-dense and spatially-sparse in comparison to space-based XCO_2 observing instruments. On sub-seasonal scales the most significant variations in simulated XCO_2 are driven by synoptic-scale advection (occurring over 1000s of km and lasting a few days to weeks) of continental-scale spatial XCO_2 gradients, as opposed to local flux variability (Keppel-Aleks et al., 2011). Specifically, local fluxes are not the dominant influence on TCCON XCO_2 variability, even on diurnal timescales. Sub-seasonal variations in midlatitude TCCON XCO_2 are primarily driven by synoptic-scale advection across the hemispheric summertime north-south gradient in XCO_2, shaped by the mean distribution of growing season biosphere carbon uptake (Keppel-Aleks et al., 2012). Synoptic-scale TCCON XCO_2 variability could reach up to half the peak-to-trough amplitude of the seasonal cycle. XCO_2 variability at midlatitude TCCON sites differed during the summer based on the strength of the north-south gradient in the area (Keppel-Aleks et al., 2012). Outside of summer months, synoptic XCO_2 variability is more similar across midlatitude TCCON sites when the gradient is weaker. Significant sub-seasonal variability in TCCON XCO_2 is also attributed to advection by mesoscale weather systems (occurring over ~10s km and lasting one day or less). Mesoscale variability at TCCON sites is typically between 0.2 ppm and 0.5 ppm, 30% to 50% the magnitude of synoptic-scale variability (Torres et al., 2019). The observed

mesoscale variability was about half the magnitude of diurnal fluxes at Northern Hemisphere midlatitude TCCON sites but could be greater in magnitude than diurnal variability outside the growing season.

The temporal duration of individual OCO-2 overpasses is too short and the repeat cycle of OCO-2 orbits is too long to sample synoptic or mesoscale systems' time-variability directly. The satellite has a repeat cycle of 16 days, acquiring at each time step a narrow swath of up to eight cross-track samples that have individual spatial footprints of 2.4 km along-track by 1.25 km cross-track. While synoptic-scale atmospheric transport is often explicitly resolved in inversion techniques, simulation of mesoscale transport is less common and errors/gaps in coverage inhibit OCO-2 XCO_2's ability to capture real local gradients. For instance, clouds that obscure OCO-2 measurements are often present in mesoscale weather systems. Some inverse frameworks have improved the spatial resolution of transport models to simulate mesoscale atmospheric transport despite the great required computational expense (Wesloh et al., 2020), but inversions on this scale require accurate representations of subgrid-scale spatially coherent variability in assimilated XCO_2.

To verify fine-scale variability in OCO-2 XCO_2, recent studies have compared observed variability with simulated XCO_2 or high-resolution validation XCO_2 collected from in-situ sites or aircraft. Torres et al. (2019) used space for time substitution to characterize the influence of mesoscale transport on OCO-2 v8 XCO_2 by comparing high-pass-filtered ($<$250 km) along-track spatial XCO_2 variations to temporal mesoscale variations in TCCON XCO_2. They observed greater spatially coherent along-track variability in OCO-2 XCO_2 than what could be attributed to mesoscale transport (~0.4 ppm along 250 km of orbit track). Combined with correlation length scales much shorter (~10–30 km) than those associated with mesoscale systems, they concluded

systematic bias contributes significant along-track spatially coherent variability to OCO-2 v8 XCO_2. Baker et al. (2022) found similar OCO-2 v10 XCO_2 error correlation length scales of 20 km and ~10km, noting the two distinct length scales that fit much of the data may be driven by different sources of error (fast-changing errors related to surface parameters versus slow-changing errors related to atmospheric parameters). Bell et al. (2020) compared along-track OCO-2 v9 XCO_2 variations with aircraft underflights equipped with a Multifunctional Fiber Laser Lidar (MFLL). They found agreement between OCO-2 and MFLL on synoptic scales but disagreement on local scales (0.35 correlation with MFLL), supporting the finding that systematic errors contribute significant spatially coherent non-transport structures at fine scales in OCO-2 XCO_2. Worden et al., (2017) used the NASA GMAO high-resolution free-running GEOS-5 CO2 simulation to estimate natural fine-scale variability in XCO_2 (owing to wind or fluxes) and compared that to observed variability in OCO-2 V7 XCO_2 occurring along 100 km of orbit track. They found larger observed variability than simulated natural variability occurring over that small ~100 km neighborhood (simulated variability was ~0.1 ppm and observed variability was ~1.28 ppm). These studies have shown real signals driven by mesoscale transport or fluxes are entangled with fine-scale correlated errors in OCO-2 XCO_2. Fine-scale variability and correlations must be explicitly represented in inverse model frameworks or used to inflate observation error estimates. Model misrepresentation of subgrid-scale variability can impart errors in inverted fluxes on urban to global scales (Chevallier , 2007; Lauvaux et al., 2016; Corbin et al., 2008).

The effect of spatially coherent biases on inverted flux uncertainty is largely dependent on the spatial and temporal scale of the bias and aggregation scheme. When assimilating XCO_2 into inversions, soundings are often averaged over some distance of orbit track, typically close to

the length of a model grid cell (for example, ~110 km for a 1x1 degree grid). Standard error

estimates of the aggregated data are then used to evaluate model biases. For example, Hu et al.

(2020) evaluated biases in monthly mean high-resolution WRF-VPRM model-simulated XCO_2

to time-matched OCO-2 v9 XCO_2 data pairs aggregated in 1x1 degree grid boxes. Dong et al.

(2021) used OCO-2 v9 data integrated onto a weather-biosphere-online-coupled model WRF-

Chem and CarbonTracker 2019 grids (20 km grid and 1 x 1 degree grids, respectively) for

validation of simulated XCO_2. Byrne et al. (2021) used OCO-2 v10 XCO_2 to optimize fluxes

from the NASA Carbon Monitoring System – Flux (CMS-Flux) inversion at 2 x 2.5 degree

spatial resolution. In the OCO-2 v9 Model Intercomparison Project (MIP), XCO_2 were averaged

along 10 s spans of orbit track (~70 km) before assimilation into the inverse model, assuming

errors were not correlated within the 10 s span (Peiro et al., 2022). XCO_2The assumptions made

about the data and employed in bias correction are made due to the long decorrelation length of

atmospheric CO_2 (500-1000 km) (Chevallier , 2007). However, observed XCO_2 correlation

lengths are much shorter than these typical averaging lengths, resulting in correlated groups of

data and error within the aggregate (Torres et al., 2019, Baker et al., 2022). Making false

assumptions about the independence of each along-track XCO_2 sounding and its associated error

leads to overconfidence in the XCO_2 and incorrect error reductions (Baker et al., 2010).

Recent studies have tried to address fine-scale error correlations to varying degrees, but

challenges remain in representing and attributing the uncertainty they produce in inverted fluxes.

Intermediate averaging, such as averaging 1s or 2s spans before averaging the full 10 s span, was

tried in the v7 MIP (Crowell et al., 2019) and shown to improve aggregate error estimates (Baker

et al., 2022). Using Lidar MFLL underflight validation data, Baker et al. (2022) evaluated flux

errors that arise from representing measurement and error correlations in v10 XCO_2. They

employed an Observing System Simulation Experiment (OSSE) and found retrieval biases were much larger and more variable than parameterized biases and derived a 1D error estimation model that represented correlations between the data as exponentially decaying. The error model showed improvement upon constant correlation models such as that used in the V9 MIP, which set constant correlation coefficients of +0.3 for adjacent land retrievals and doubled this value to +0.6 for adjacent ocean retrievals. While the constant correlation model proved to be sufficient, the correlation coefficients are somewhat arbitrary. Baker et al., (2022) also used this twice-the-land relationship to double correlations over the ocean in their model because they did not have MFLL data over the ocean. Due to lacking validation data and assumptions that XCO_2 statistics over the ocean should be fairly uniform, XCO_2 correlation lengths over the ocean have typically been approximated using correlations that have been better characterized in retrievals over land. Correlations in OCO-2 XCO_2 imparted by systematic bias have not been explicitly studied to the extent needed to represent aggregate uncertainty in flux inversions.

Identifying sources of error in OCO-2 XCO_2 and correcting systematic biases is an ongoing effort. In bias correction, systematic error in XCO_2 that correlates with retrieval parameters (for example, aerosol quantities, albedo, or surface pressure) is corrected using multivariate regression. Improvements in the retrieval algorithm and parametric bias correction reduce these biases with each data release (Wunch et al., 2011; Wunch et al., 2017; O'Dell et al., 2018; Kulawik et al., 2019; Kiel et al., 2019). Wunch et al. (2017) found generally good agreement with v7 XCO_2 and TCCON validation data at global scales (RMS differences less than 1.5 ppm) but noted that significant spurious variability remains on local scales. Residual biases are greater above 45° N, over areas subject to pathlength errors due to scattering from clouds or aerosols, and over areas where errors in assumed surface pressure arise due to rough

topography (Wunch et al., 2017). Erroneous surface pressure estimates can also occur in the meteorological reanalysis used in bias correction when sampled at incorrect times or if there are small misspecifications of instrument pointing, particularly over regions with rough topography (Kiel et al., 2019). Despite improvements in the retrieval algorithm, systematic biases over regional and finer scales in the latest version (v10) XCO_2 can be large enough to impede surface flux estimation. Rastogi et al. (2021) compared bias-corrected v10 XCO_2 retrievals with in situ data-constrained simulated XCO_2 over North America. They found differences between the retrieved and simulated quantities on local scales (tens of kilometers) of the same magnitude as the imprint of surface fluxes in the total column and were able to attribute these differences to persisting fine-scale systematic errors in XCO_2. Error analysis and uncertainty quantification remain areas of active research that strive toward reaching the level of accuracy and precision required for XCO_2 measurements to detect exceptionally subtle flux-driven variations in the atmospheric column.

Until the variance budget is fully resolved and applied within inverse modeling frameworks, the representation of aggregated OCO-2 XCO_2 will cause large uncertainties in inverted fluxes on regional and sub-seasonal scales. To understand the influence of atmospheric transport, surface processes, and error on different spatial and temporal scales, we characterize variability in OCO-2 v10 XCO_2 over North America and adjacent ocean basins. We evaluate spatial patterns in seasonal and synoptic-scale variability that illustrate the relative impact of atmospheric circulation and surface flux gradients on XCO_2 on different scales. On mesoscale and finer scales, we conduct an along-track geostatistical analysis of variability to reveal possible retrieval errors and improve the representation of aggregated XCO_2 and associated uncertainty in inverse frameworks. Relationships between variability and season, surface type, and pointing

mode help narrow down the specific processes driving real and spurious XCO_2 variability. Our analysis provides insight into both the dynamics of atmospheric CO_2 and the applications and limitations of XCO_2 measurements.

2 Materials and Methods

2.1 Characterizing Seasonal and Sub-seasonal Variability in XCO_2

We use the OCO-2 Lite Level 2 data product, which provides geolocated, bias-corrected XCO_2 aggregated into daily files. OCO-2 spectrometers collect 24 spectra per second and yield over 100,000 XCO_2 observations each day, about 10% of which are sufficiently cloud-free scenes and have the precision required for scientific applications. We include all XCO_2 soundings marked with a "good" quality warning flag from September 2014 to December 2019 and spanning between 180° W - 30° W and 14° N - 89° N. This study domain encompasses North America and extends into the adjacent Pacific and Atlantic Ocean basins. XCO_2 is derived from version 10 (V10) of the Atmospheric Carbon Observations from Space (ACOS) retrieval algorithm (O'Dell et al., 2012, 2018), and results include soundings collected in glint and nadir observation modes. We characterize average seasonal and sub-seasonal variability in XCO_2 within bins spanning 5° latitude and longitude. Results are compared by observation mode, season, and biome in Section 3. We use a TransCom regional mask that divides the domain into boreal, temperate and tropical regions of N.A., the North Pacific, and the North Atlantic, publically available by the current OCO-2 V10 MIP (Figure S1 in the Supporting Information). Across the study domain, there are about ~500,000 – 700,000 observations per month, with fewer observations (~300,000 – 500,000) in December, January, and February.

We compute a series of anomalies to characterize v10 XCO_2 variability on seasonal and sub-seasonal scales (Figure 1a). First, we detrend the long-term anthropogenic temporal increase in XCO_2 using a linear regression computed on the time series of all XCO_2 in the domain ($\bar{X}$). We subtract the long-term temporal trend $\bar{X}$ from the XCO_2 time series and remove the detrended mean of each box $\langle X \rangle$ from the corresponding XCO_2 in equation (1).

(1)

$$X' = X_{raw} - \bar{X} - \langle X \rangle$$

From the resulting detrended, spatial annual anomalies (denoted as X'), we compute the average seasonal cycle for each bin in equation (2) (Figure 1b). We fit the mean annual cycle of each bin with a 1st and 2nd harmonic (X_a). Average seasonal amplitudes for each bin are computed as the peak-to-trough difference of X_a. To account for additional interannual variation, we compute a 6-month low-pass filter on annual anomalies (X_{lp}). Sub-seasonal XCO_2 anomalies, X'', are calculated by removing the annual cycle and low-pass filter from X' (equation (3)).

(2)

$$X_a = X'(t, b) = b_1 \sin\big(2\pi(t + b_2)\big) + b_3 \sin(4\pi(t + b_4))$$
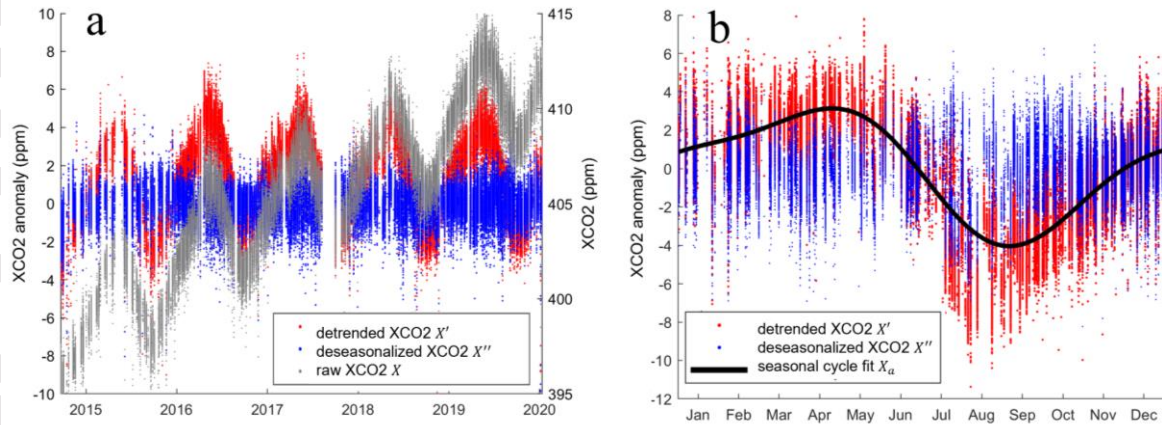
(3)

$$X'' = X' - X_a - X_{lp}$$

Figure 1. For each 5° bin, raw XCO_2 is detrended to compute a series of anomalies. For a bin over Hawai'i, we show (a) time series of raw XCO_2, annual X' and sub-seasonal X'' XCO_2 anomalies. (b) X'' are computed by removing the spatial bin means $\bar{X}$, the low-pass filter representing interannual variability X_{lp}, and the mean annual cycle of annual XCO_2 anomalies X_a. Note: (b) shows the full XCO_2 timeseries grouped by month, not the average over all years. Data density was lower earlier in the mission (fewer than 500,000 observations per month in 2014 and 2015) as sampling patterns, decontamination cycling, calibration, and ground station communication were being optimized. Starting in the summer of 2015, the OCO-2 team employed the V7/7r algorithm to reprocess the data record and develop corrections for these different issues, summarized in Crisp et al. (2017)." The large gap in observations spanning late July 2017 through September 2017 occurred due to band tracking and potentiometer issues, leading to an instrument reboot and extended period during which XCO_2 data was not created or invalid.

2.2 Geostatistical Analysis of Fine-Scale Variability in XCO_2

We use geostatistical methods to characterize the magnitude and spatial coherence of variability in XCO_2 on two sub-seasonal scales corresponding to synoptic and mesoscale atmospheric circulation because sub-seasonal variability in XCO_2 is largely driven by atmospheric transport. We divide sub-seasonal variability into synoptic and finer scales as variability in X'' occuring on spatial scales longer and shorter than 250 kilometers. Torres et al. (2019) demonstrated the 250 km spatial cutoff isolates mesoscale and finer variability in OCO-2 XCO_2 from synoptic-scale variations. We compute a 250 km low-pass filter on X'' along each orbit track (Figure 2a) using the spherical distance between two coordinates on Earth's surface as distance along orbit. To apply the filter, up to 8 cross-track soundings were centered onto a one-dimensional track and gap-filled using 1-D linear interpolation on a spherical surface. Variations passed by the 250-km digital low-pass filter are subtracted from XCO_2 in their original position to compute fine-scale XCO_2 anomalies that capture variations on the atmospheric mesoscale (Figure 2b).

For each orbit pass through a 5° bin, we compute the experimental and theoretical semivariogram for fine-scale XCO_2 anomalies (Figure 2c). The experimental semivariogram, $\gamma(h)$ (equation (4)), measures how related two points are to one another at different separation (lag, h) distances (Cressie, 1993). We compute the average semivariance for a total number of pairs N at 50 lag distances h centered between 0 and 100 km. An orbit has sufficient observations to compute the semivariogram if the spatial span of the retrievals in a 5x5 degree bin is at least 100 km along-track and there are at least 50 good observations for each along-track step (up to 8 cross-track footprints are retrieved for each along-track step). X_k and X_{k+h}

represent the fine-scale XCO_2 anomaly at locations k and $k + h$. We fit each experimental

semivariogram with a spherical model (equation (5)) to compute the theoretical semivariogram

(Figure 2c). The theoretical semivariogram estimates the total sample variance (sill, c_∞), the

random variance (nugget, c_0), the resolved variance (sill minus nugget, c_s), and the length at

which two soundings become independent (range, a_{space}).

(4)

$$\gamma(h) = \frac{1}{2N(h)} \sum_{k=1}^{N_h} [X_k - (X_{k+h})^2]$$

(5)

$$\gamma(h) = \begin{cases} c_0 + (c_\infty - c_0)(\frac{3h}{2a_{space}} - \frac{1h^3}{2a_{space}^3}) \; for \; h \geq a_{space} \\ c_\infty \; for \; h < a_{space} \end{cases}$$

From all modeled parameter estimates and associated errors, we compute weighted

averages of c_∞, c_0, and a_{space} for each bin (equation (6)) using two approaches. The variable x

represents the modeled parameter estimate (c_∞, c_0, or a_{space}) and the variable σ^x represents

error in estimated c_∞, c_0, or a_{space}. Because errors scale with the magnitude of estimated

parameters, we computed averages using the inverse of error (σ) as well as the proportionate

error (σ/x). Weighted averages computed from the two approaches were only significantly

different for range estimates (Section 3), and we present results computed using inverse error.

Average spatially coherent fine-scale variance, $\langle c_s \rangle$, is calculated in equation 7 as the random

variance subtracted from the average total variance.

(6)

$$\langle a_{space} \rangle, \langle c_0 \rangle, \langle c_\infty \rangle = \bar{x} = \frac{\sum_{i=1}^{N} x_i * \frac{1}{\sigma_i^x / x_i}}{\sum_{i=1}^{N} \frac{1}{\sigma_i^x / x_i}}$$

(7)

$$\langle c_s \rangle = \langle c_\infty \rangle - \langle c_0 \rangle$$

We use error estimates computed from the spherical model to assess the goodness of fit of each modeled parameter to the experimental semivariogram. If error for each estimated c_∞, c_0, a_{space} is larger than the value of the estimated parameter, we omit those poorest fits from the computation of the total bin averages. The majority of errors on included c_∞ were less than 10% the parameter value, ~10% of the estimated c_0 parameter, and less than 30% of the estimated a_{space} parameter. Using inverse error to weight the parameters ensured that the results we present can be interpreted in good confidence because values with the best spherical model fits are given more weight than values with poorer spherical model fits.

Average synoptic-scale variance for each bin is computed as the remainder of total sub-seasonal variance after subtracting average total fine-scale variance $\langle c_\infty \rangle$. To compare variance by surface type, we repeat the geostatistical analysis using orbit passes over either majority land, water, or mixed surface types. We present our results in terms of variability, the square root of spatially coherent and random variance: $\langle c_\infty \rangle^{1/2}$, $\langle c_s \rangle^{1/2}$, and $\langle c_0 \rangle^{1/2}$.
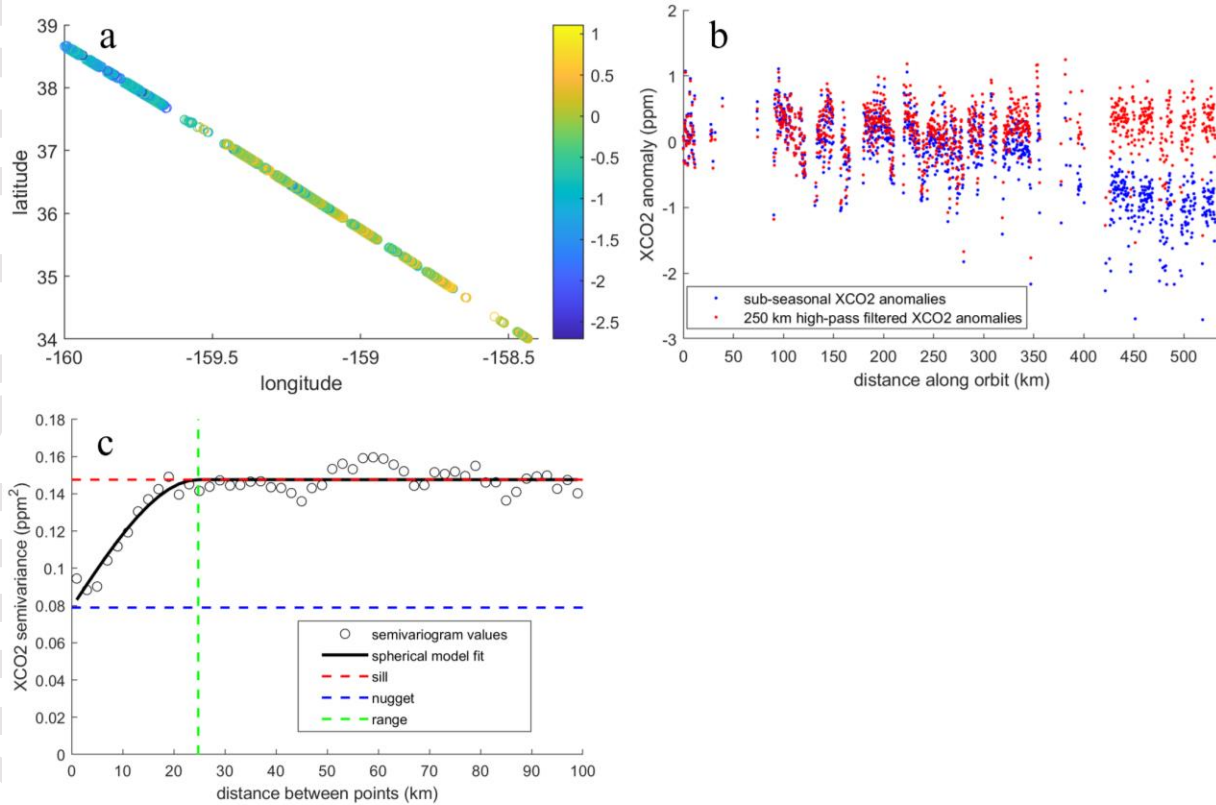
Figure 2. (a) Sub-seasonal XCO$_2$ anomalies X'' collected within a 5° bin during one orbit pass are (b) high pass filtered to remove variations occurring on spatial scales longer than 250-km to isolate mesoscale and finer variations. (c) The average semivariance of high pass filtered X'' anomalies for 50 lag distances between 0 and 100 km is measured by the experimental semivariogram and fit with a spherical model. The theoretical semivariogram estimates the total sample variance (sill, c_∞), the random variance (nugget, c_0), the resolved variance (sill minus nugget, c_s), and the length at which two soundings become independent (range, a_{space}).

3 Results & Discussion

3.1 Mean Spatial XCO_2 Anomalies

Mean spatial anomalies by season (Figure 3) indicate where average XCO_2 concentrations were relatively enriched (positive) or depleted (negative) from 9-2014 to 12-2019 compared to the domain mean. During the summer (June, July, and August), there is a large increasing gradient of ~4 ppm from north to south, centered around 39° N. Summertime anomalies exhibit the most pronounced gradient across all seasons and most closely follow mean zonal circulation. During the fall (September, October, and November), XCO_2 anomalies across the domain are negative, with the most negative anomalies occurring above 54° N. There is an east-west contrast across the continent where greater detrended XCO_2 concentrations occur over the western U.S. and adjacent Atlantic Ocean and lower detrended XCO_2 occur over the western U.S. and tropics. During the winter (December, January, and February), anomalies across the domain are positive and the same east-west contrast is present (lower anomalies to the western U.S. and tropics and greater anomalies to the eastern U.S.). Over the ocean, there is a decreasing north-south gradient in anomalies. Certain high latitude bins are omitted due to OCO-2's wintertime data collection gaps. Anomalies are most positive during the spring (March, April, and May). The most negative anomalies occur over the boreal continental region (Table 1). The most positive anomalies occur over the northern Pacific temperate region. Average seasonal anomalies are compared by region in Table 1.

Mean seasonal anomalies exhibit an annually reversing north-south gradient shaped by zonal circulation of north-south distribution of surface fluxes. During the summer, there is greater carbon uptake by the terrestrial biosphere in higher latitudes, creating an increasing

north-south gradient bounded by the jet stream. During the winter, respiration outweighs photosynthesis and fossil fuel emissions are concentrated in higher latitudes, creating a decreasing north-south gradient. Summertime anomalies follow dominant wind patterns and constant potential temperature surfaces at 700 hPa. Outside of summer months, east-west contrasts over the continent suggest the influence of meridional flow. High velocity westerly winds travel south over the coastal Pacific adjacent to the west coast, diverting air away from the continent. The east-west contrasts we observe could also be influenced by easterly trade winds deflecting off the North Pacific High, a semi-permanent subtropical anticyclone, and circulating lower latitude air northward along the western continent. During the springtime, we observe the largest land-ocean contrast in XCO_2 at the west coast boundary (XCO_2 over 2 ppm greater over the Pacific Ocean than immediately across the coastline). We expect patterns to reflect mean atmospheric patterns and the large-scale north-south carbon flux distribution rather than local underlying carbon fluxes due to rapid horizontal mixing in the free troposphere and XCO_2's large footprint. Consequently, the magnitude and sharp boundary of this land-ocean difference is difficult to interpret, given that underlying fluxes over the continent are larger and more seasonally variable than those over the adjacent ocean. Ongoing discussion in the OCO-2 community focuses on differences between land and ocean XCO_2 observations. These results prompt investigation into whether the divergence of easterly and westerly winds, a land-ocean retrieval bias, or systematic bias related to underlying surface properties are driving land-ocean XCO_2 differences across the west coast, particularly during spring months.
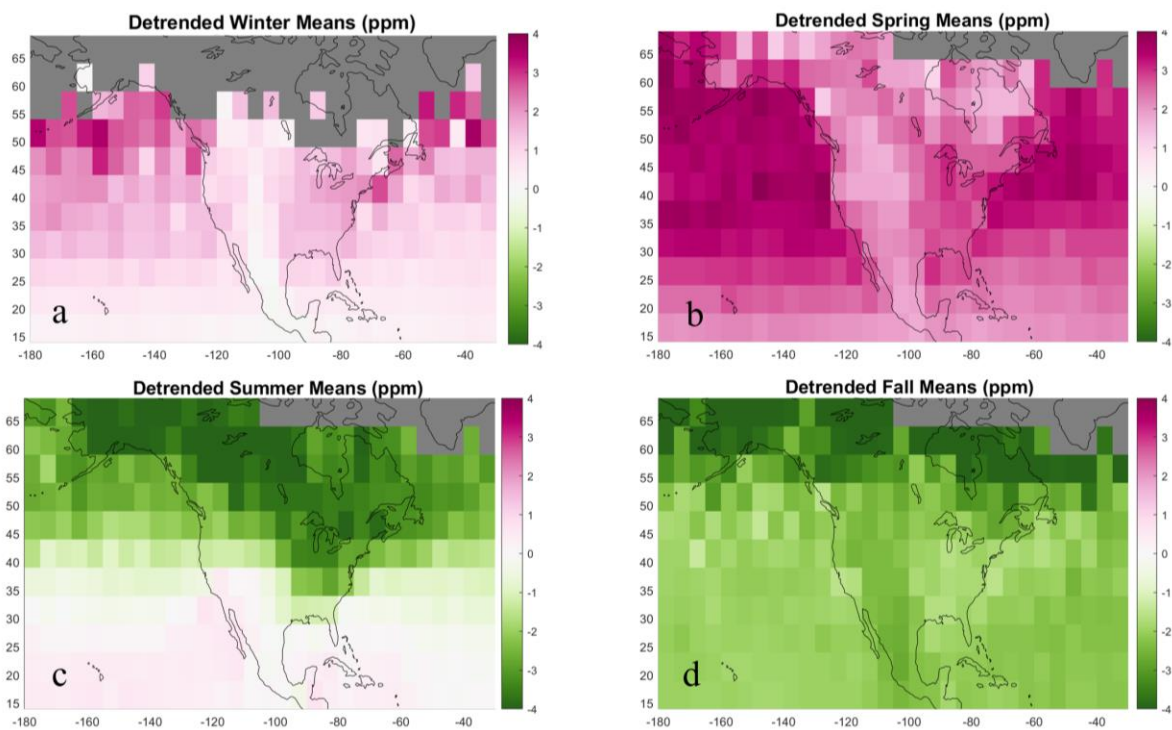
Figure 3. Long term temporally detrended anomaly averages for winter (a), spring (b), summer (c), and fall (d).

3.2 Seasonal Variability in XCO_2

We present the average peak-to-trough amplitude (Figure 4a) and phasing (Figures 4c-d) of the mean seasonal cycle in XCO_2 (X_a). Seasonal amplitudes generally increase with latitude while also exhibiting substantial east-west variation over the continent. The greatest amplitudes (reaching 11.5 ppm) are concentrated from the highest latitudes over the Northern Ocean and boreal continental region (Table 1) to a meandering southern boundary that follows the jet stream and gradient in potential temperature θ at 700 hPa, a dynamical tracer in the free troposphere computed using Poisson's equation and 700 mb temperatures provided in the OCO-2 lite files

(Figure 4b). Land and ocean tropical regions have the lowest amplitudes on average, forming a north-south gradient of ~5 ppm. Seasonal amplitudes also decrease on average from west to east, from the North Pacific Temperate region (7.6 ppm) to the continental Temperate region (7.1 ppm) to the North Atlantic Temperate region (6.8 ppm). The exception to these large-scale patterns occurs over the western U.S, which has the lowest amplitudes in the domain (under 5 ppm). A sharp land-ocean contrast in amplitudes manifests across the western coastline; bins over the western continent have distinctly lower amplitudes (up to 4 ppm) than the adjacent bins over the coastal Pacific. This feature may be driven by transport, with greater and lesser potential temperature (Figure 4b) over the Pacific Northwest and adjacent Pacific Ocean, respectively. Alternatively, this feature may be caused by low biases in retrievals over the western continent and prompts further investigation.

Across the domain, the maximum in X_a occurs between April and May (Figure 3c) and the minimum occurs between August and October (Figure 3d). Bins with greater amplitudes in Figure 3b tend to reach an earlier maximum and minimum than bins with lower amplitudes. The seasonal cycle in XCO_2 lags behind that of surface fluxes due to the time required for surface fluxes to mix into the free troposphere, enabling OCO-2 XCO_2 to capture both extrema of the seasonal cycle even in many locations with wintertime data gaps. The root mean square error of X_a, representing average deviation from the average annual cycle fit, was 2.7 ppm on average and ranged from 0.5 ppm to 4.4 ppm, scaling with amplitude.

Spatial patterns in X_a seasonal amplitudes resemble average zonal circulation winds rather than patterns in underlying surface flux seasonality, supporting findings from Keppel-Aleks et al. (2011) that the seasonal cycle in XCO_2 is shaped by the large-scale north-south flux distribution. The spatial pattern we observe is consistent with XCO_2 amplitudes modeled by

Sweeney et al. (2015), who showed the high-latitude feature of greater amplitudes extends across the globe. Areas such as the Arctic tundra with large seasonal amplitudes despite having small biospheric and anthropogenic fluxes are influenced by transported fluxes. Zonal transport of highly seasonal fluxes from boreal regions has been used to explain increasingly large seasonal cycles in column CO_2 over the Arctic (Keppel-Aleks et al., 2011, 2012; Olsen and Randerson, 2004). Sweeney et al., (2015) suggested that northward transport from lower latitudes, in addition to zonal transport of boreal fluxes, contributes to large seasonal cycle amplitudes observed in high latitudes. Western U.S. anomalies that depart from mean zonal circulation in Figure 3a suggest the influence of meridional transport along the western continent, which could carry northwestern U.S. fluxes and the imprint of their seasonality to higher latitudes. Average characteristics of seasonal variability are compared by region in Table 1.
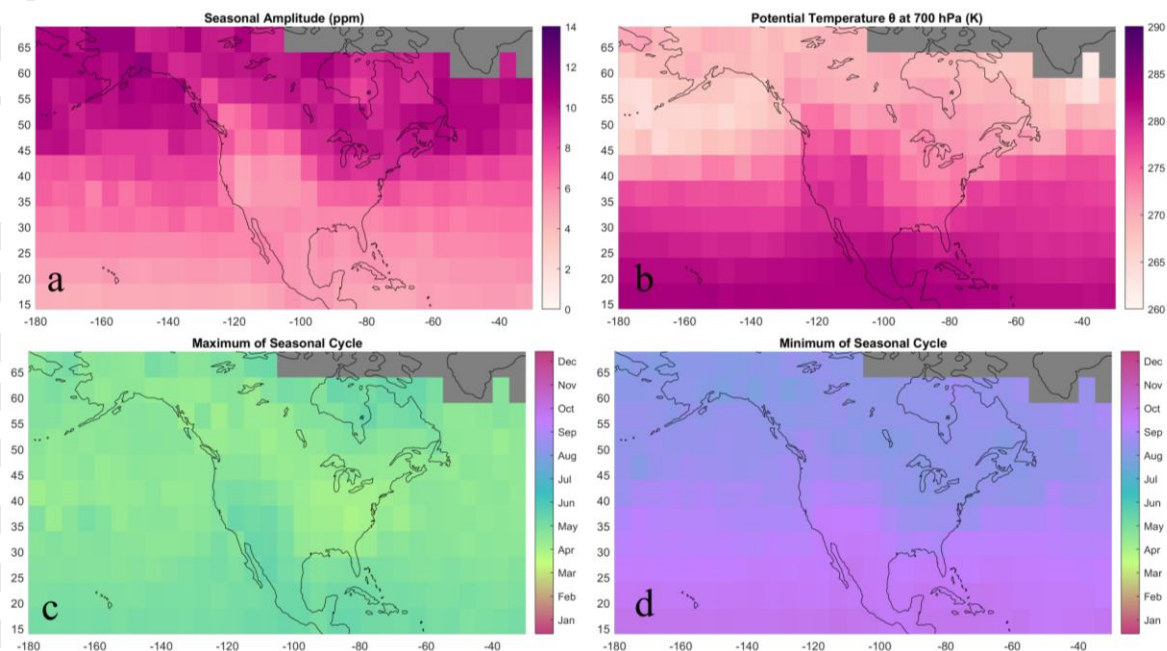
Figure 4. (a) Average peak-to-trough seasonal cycle amplitudes follow mean wind patterns and spatially correlate with changes in (b) average potential temperature at 700 hPa. The seasonal cycle reaches a maximum (c) between April and May and a minimum (d) between August and October. Bins with greater amplitudes generally reach an earlier seasonal cycle maximum and minimum.

Table 1: Average XCO_2 anomaly by season and characteristics of seasonal variability compared by region.

	Winter mean (ppm)	Spring mean (ppm)	Summer mean (ppm)	Fall mean (ppm)	Seasonal amplitude (ppm)	Seasonal maximum (decimal yr)	Seasonal minimum (decimal yr)
N. A. Boreal	1.0	2.3	-3.8	-3.7	9.8	0.36	0.66
N Pacific Temperate	1.5	3.3	-0.9	-2.1	7.6	0.36	0.72
W Pacific Tropical	0.2	2.1	0.5	-1.9	4.6	0.39	0.79
E Pacific Tropical	0.2	2.1	0.3	-2.0	4.9	0.39	0.78
N. A. Temperate	1.0	2.4	-1.8	-2.2	7.1	0.35	0.70
Northern Ocean	2.4	2.8	-3.0	-3.7	9.9	0.37	0.67
N Atlantic Temperate	1.0	2.9	-0.7	-2.1	6.8	0.36	0.73
Atlantic Tropical	0.3	2.1	0.2	-2.1	5.1	0.39	0.78
Tropical S.A.	0.2	2.1	0.2	-2.1	5.3	0.40	0.77
All	1.2	2.8	-1.6	-2.5	7.7	0.37	0.75

3.3 Synoptic-scale Variability in XCO_2

Average synoptic-scale variability in XCO_2, computed as average sub-seasonal anomaly variability occurring on spatial scales longer than 250 km, and fine-scale variability (<250 km) comprise total sub-seasonal variability in XCO_2 The components of fine-scale variability are summarized in Table 2. In Table 3, synoptic variability and fine-scale variability are compared by region. Average synoptic variability was greatest over the continental Boreal region, reaching a maximum of1.5 ppm along the west coast of Canada. Over the continent, synoptic variability decreases on average from the Boreal region to the tropics, but a cluster of greater variability also occurs over eastern bins in the Temperate region. Over the ocean, synoptic variability exhibits more uniform latitudinal patterns and is greater (over 0.5 ppm) in middle and high latitudes. Synoptic variability was lowest (under 0.5 ppm) over the subtropical and tropical ocean.

Synoptic variability exhibited a strong seasonal and moderate surface type dependence. The greatest variability occurred during the summer months over the continental midlatitudes in a northwest to southeast pattern (Figure 5b). This pattern is similar to the gradient in mean spatial summer anomalies (Figure 3c) and average potential temperature, both illustrating mean atmospheric circulation. Outside of the summer, synoptic variability is lower on average and more uniform across the domain, decreasing into the fall and reaching a minimum over both the continent and ocean during the winter and spring. On average, summertime synoptic variability was 1.0 ppm for dominantly continental bins compared to dominantly marine bins, which were 0.5 ppm on average. The land-ocean difference was most pronounced in the tropics. Synoptic variability in mixed surface type coastal bins was typically 0.2 ppm – 0.5 ppm greater when computed using observations over land versus when we only used observations over water.

Though smaller in magnitude, we still observe regional patterns of increased variability in soundings over water coastal bins, supporting they are not entirely driven by a land-ocean bias.

Our results support findings from Keppel-Aleks et al. (2011) that XCO_2 variations on the atmospheric synoptic-scale are driven by disturbances of continental-scale XCO_2 gradients rather than underlying surface flux variability. During the summer, great synoptic-scale XCO_2 variability exceeding 2 ppm occurs at the boundary of southern CO_2-enriched and northern CO_2-depleted air (refer to the asymmetrical northwest-southeast spatial XCO_2 gradient of ~4 ppm in Figure 3c). The location of increased variability correlates with the mean gradient in potential temperature θ at 700 hPa (Figure 4b), above which XCO_2 depleted air caused by growing season drawdown follows large scale atmospheric circulation patterns. Synoptic advection across the pronounced XCO_2 gradient creates a northwest-southeast trending band of high synoptic variability due to the difference in XCO_2 concentrations on either side of the large scale circulation-driven gradient. Because greater differences between XCO_2 to the north and south increase synoptic-scale variability, greater synoptic-scale variations could reflect greater carbon fluxes into the northern biosphere. Outside the midlatitudes, synoptic variability does not exhibit the same seasonality. In the high latitudes, synoptic variability is greater outside of summer months when climatological cyclone frequency is greater. In the subtropics and tropics, synoptic-scale variability is greater around the continent where there is zonal disruption in wind direction (Figure S2 in the Supporting Information). Differences in air from the westerlies transported south along the western side of the continent and air carried by the trade winds could drive synoptic XCO_2 variability in this area.
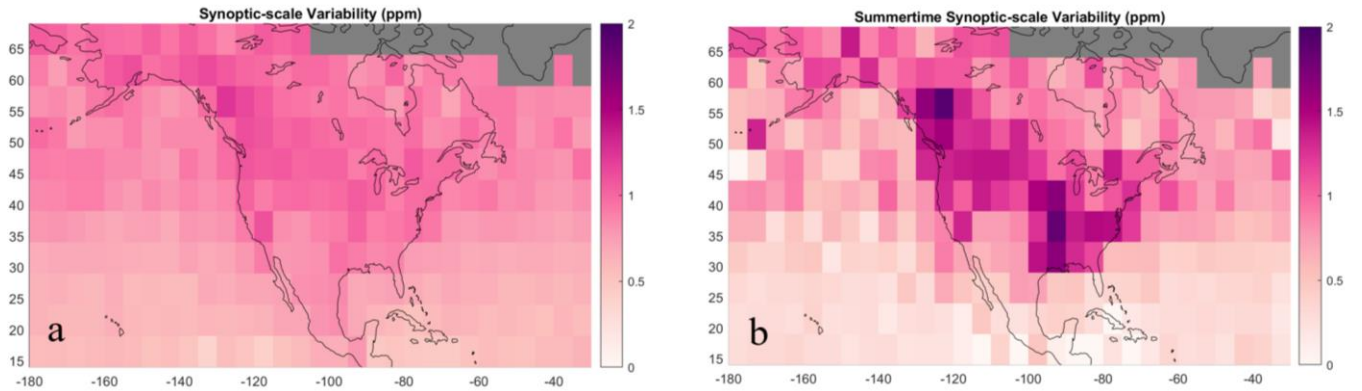
Figure 5. (a) Average synoptic-scale variability. (b) Average synoptic-scale variability during June, July, and August. We note that more scatter in summertime synoptic-scale variability is caused by less data to compute the average; it does not indicate real features of variability changing over small scales.

3.4.1 Fine-scale Variability in XCO_2

Fine-scale variability (computed as total along-track variability occurring on spatial scales shorter than 250 km) and synoptic-scale variability comprise total sub-seasonal variability in XCO_2. In the following sections, we partition total fine-scale variability $\langle c_\infty \rangle^{1/2}$ into two components: spatially-coherent and random variability. Spatially coherent fine-scale variability, $\langle c_s \rangle^{1/2}$ (Section 3.4.1) in XCO_2 reflects variations driven by fine-scale transport, flux variability, or systematic bias. Random fine-scale variability, $\langle c_0 \rangle^{1/2}$, (Section 3.4.3) reflects instrument noise. In Section 3.4.2, we quantify the average geostatistical spatial range, $\langle a_{space} \rangle$, the distance at which two points become independent. $\langle a_{space} \rangle$ quantifies the average length scale of mechanisms driving spatially coherent fine-scale variability in XCO_2.

These parameters are relevant to flux inversion because errors present in spatially-coherent fine-scale variability $\langle c_s \rangle^{1/2}$ cannot be effectively reduced by averaging multiple soundings like random fine-scale variability $\langle c_0 \rangle^{1/2}$ (noise). Fine-scale spatially-coherent variability can be substantially larger than reported sounding errors alone and the coherent mesoscale signal (Torres et al., 2019), leading to large representation errors in inverse modeling that have been shown to arise when mesoscale variations are not accurately constrained (Corbin et al., 2008). The geostatistical range $\langle a_{space} \rangle$ will inform modelers the distance at which XCO_2 observations become independent of one another, which shapes the degrees of freedom in the computation of aggregate standard error. We present average characteristics and spatial patterns in these geostatistical metrics to help modelers understand the fine-scale statistics of XCO_2 and how they change across the domain or by season. At the end of Section 3.4.3, a comparison of these parameters for XCO_2 collected in nadir or glint observation mode in five continental bins (Table 3) shows only minimal differences between the two modes. The comparison is limited to continental bins because nadir mode observations are only collected over land.

Table 2. Description of geostatistical parameters presented in Section 3.4.

Symbol	Long Name	Description
$\langle c_\infty \rangle^{1/2}$	Total fine-scale variability	Average total fine-scale (<250 km) variability estimated from the sill (where semivariance levels off at the decorrelation length) of spherical fits to the semivariogram

$\langle c_s \rangle^{1/2}$	Spatially-coherent fine-scale variability	Average correlated fine-scale (<250 km) variability estimated from the partial sill of spherical fits to the semivariogram (sill – nugget)
$\langle c_0 \rangle^{1/2}$	Random fine-scale variability	Average random fine-scale (<250 km) variability estimated from the nugget (y-intercept) of spherical fits to the semivariogram
$\langle a_{space} \rangle$	Geostatistical range	Decorrelation length estimated from the distance at which the slope of the spherical model fit to the semivariogram levels becomes 0.

Table 3. Average characteristics of sub-seasonal XCO_2 variability; synoptic, synoptic variability during the summer months (June, July, and August) and total fine-scale variability $\langle c_\infty \rangle^{1/2}$ compared by biome.

	Synoptic variability (ppm)	Synoptic Variability JJA (ppm)	$\langle c_\infty \rangle^{1/2}$ (ppm)
N. A. Boreal	0.96	0.98	1.14
N Pacific Temperate	0.59	0.53	0.56
W Pacific Tropical	0.32	0.32	0.51
E Pacific Tropical	0.3	0.23	0.58
N. A. Temperate	0.9	1.12	0.85

Northern Ocean	0.79	0.74	0.70
N Atlantic Temperate	0.53	0.54	0.55
Atlantic Tropical	0.29	0.23	0.53
Tropical S.A.	0.37	0.11	0.77
All	0.68	0.69	0.71

3.4.2 Total Fine-scale Variability in XCO_2

Average fine-scale variability in OCO-2 XCO_2, $\langle c_\infty \rangle^{1/2}$, computed as total along-track variability occurring on spatial scales shorter than 250 km, ranged from 0.5 ppm to 2.1 ppm (Figure 6a). Compared to synoptic variability, $\langle c_\infty \rangle^{1/2}$ exhibited less seasonal variation and showed a much more robust dependence on surface type. We observed low and uniform $\langle c_\infty \rangle^{1/2}$ (generally between 0.5 and 0.7 ppm) over the ocean. $\langle c_\infty \rangle^{1/2}$ was greater (1.0 ppm on average) and more irregular over the continent. It also exhibits some of the same regional features as synoptic variability (great variability along the west coast of Canada) while lacking the large-scale variation with latitude.

3.4.3 Spatially Coherent Fine-scale Variability in XCO_2

Average spatially coherent fine-scale variability $\langle c_s \rangle^{1/2}$ in XCO_2 ranged from 0.4 ppm to 2.1 ppm (Figure 6b). While $\langle c_s \rangle^{1/2}$ exhibited significant spatial heterogeneity over land, $\langle c_s \rangle^{1/2}$ was robustly low and uniform over the ocean (typically 0.4-0.5 ppm). Over the continent, $\langle c_s \rangle^{1/2}$ was greatest in the boreal region (1.1 ppm on average), 0.8 ppm in the temperate region, and 0.7

ppm in the tropical region (Table 4). We observe the greatest $\langle c_s \rangle^{1/2}$ (exceeding 2 ppm) along

the west coast of Canada, twice as large as the average for all continental bins (0.9 ppm). Over

many bins in the middle of the continent over the Great Plains, adjacent interior lowlands west of

the Great Lakes, and shrublands and desert southwestern U.S.,$\langle c_s \rangle^{1/2}$ was relatively low.

Compared to synoptic-scale variability, $\langle c_s \rangle^{1/2}$ showed much greater surface type dependence

and far less seasonal dependence. Seasonal variations in $\langle c_s \rangle^{1/2}$ were ~0.1 ppm for all biomes

except the N.A. temperate region. Over the southeastern U.S., $\langle c_s \rangle^{1/2}$ was ~0.2 ppm greater

during the summer and winter. Over the north eastern U.S., $\langle c_s \rangle^{1/2}$ was ~0.4 ppm greater during

the winter. The feature of large $\langle c_s \rangle^{1/2}$ over British Columbia and the Yukon was present during

spring, summer, and fall. There was insufficient data to compute an average $\langle c_s \rangle^{1/2}$ over winter

months. We compared $\langle c_s \rangle^{1/2}$ by surface type in these coastal bins and found $\langle c_s \rangle^{1/2}$ over water

was much lower (0.5 ppm or below) compared to over land (1 ppm to 2 ppm). Our geostatistical

analysis of version 9 data also revealed this feature, equal in magnitude to the v10 results. For

other bins that had sufficient land and water retrievals for comparison, we found land-ocean

differences varied geographically. Over the east coast of Canada, $\langle c_s \rangle^{1/2}$ was generally 0.5 ppm

over water and 1 ppm over land. Over the tropical continent and islands, $\langle c_s \rangle^{1/2}$ was generally

below 0.5 ppm when computed over water. When computed over land, $\langle c_s \rangle^{1/2}$ was closer to 1

ppm and exceeded 1.5 ppm in one bin over Hawaii. Land and water $\langle c_s \rangle^{1/2}$ were most similar

over the midlatitudes. Across the full domain, there is an average land-ocean bias of 0.4 ppm.

The average $\langle c_s \rangle^{1/2}$ for bins that have greater (>50%) land surface type fractions was 0.9 ppm,

nearly twice as large as the average for bins that have greater water surface type fractions (0.5

ppm).

Across the continent, especially in the high latitudes, $\langle c_s \rangle^{1/2}$ is larger than expected for natural variations (imparted by winds or fluxes) alone (Torres et al., 2019; Worden et al., 2017). Further, we observe a distinct land-water contrast in c_s, and while fluxes are generally smaller and less variable over the ocean, it is likely the contrast is enhanced by systematic error. Larger systematic errors can occur in XCO_2 over land, where greater heterogeneity in surface properties like topography and albedo complicates retrieval. In particular, the exceptionally large $\langle c_s \rangle^{1/2}$ we observe in bins near the west coast of Canada was only present for land retrievals, prompting investigation into sources of regional systematic bias. We found that these bins also had the greatest average standard deviation of surface elevation, a variable provided in the sounding group of the OCO-2 data product (Figure S2 in the Supporting Information), suggesting a possible unresolved retrieval error related to topographic roughness. The western coast of Canada is also exceptionally cloudy, which inhibits retrieval. It is also possible the high variability is increased by a real signal related to transport as this part of the coast serves as the boundary on the atmospheric path of the jet stream between the low pressure zone in the North Pacific and higher pressure continent. We observed this feature in v9 XCO_2 as well.

3.4.4 Geostatistical Range of Fine-scale Variability in XCO_2

The geostatistical range $\langle a_{space} \rangle$ of spatially coherent fine-scale variability in XCO_2 was 16 km on average for the full domain and spanned from 7 km to 27 km (Figure 6c). $\langle a_{space} \rangle$ was spatially irregular across the domain, though slightly more coherent within a latitude circle over the ocean. The boreal region had the shortest $\langle a_{space} \rangle$ on average (11 km), followed by the

Northern Ocean (14 km) (Table 4). The southeastern U.S. had relatively short $\langle a_{space} \rangle$ (under 15 km) compared to the rest of the temperate continental region. Bins over the continental tropics also had relatively short $\langle a_{space} \rangle$. Over the ocean, $\langle a_{space} \rangle$ varied from 9 to 27 km over the tropical ocean and North Pacific, respectively. $\langle a_{space} \rangle$ over the Pacific Ocean were shorter on average and more variable than over the Atlantic Ocean. $\langle a_{space} \rangle$ could be up to twice as large when weighted using proportional error as opposed to inverse error (Equation 6) but remained below 40 km and spatial patterns were consistent.

We find shorter $\langle a_{space} \rangle$ than those expected from mesoscale weather systems, further supporting that spatially coherent error is present in XCO_2 and depresses along-track correlation lengths. For all bins, especially in high latitudes, ranges were significantly skewed, with a peak of smaller values (< 20 km) and a long tail of larger values more similar to the length scale of mesoscale systems (up to 70 km). Recent studies (Torres et al., 2019, Bell et al, 2020, Baker et al., 2022.) support that spatially coherent error depresses satellite XCO_2 ranges, particularly over land. We compared $\langle a_{space} \rangle$ computed using either majority land or water retrievals, finding $\langle a_{space} \rangle$ was significantly larger when computed over water (~10-20 km) in the tropics and midlatitudes. While ranges over the ocean were longer than those over land on average, they were equally as short (under 15 km) over the ocean in high latitudes. This suggests a retrieval covariate over the high latitude ocean is resulting in correlated error, such as cloud cover or aerosols transported from Eurasia. There was an exception for a few bins around the Hudson Bay, where $\langle a_{space} \rangle$ was longer using water retrievals. But due to data issues, this feature may not be robust; fine-scale statistics over this particular area should be interpreted with caution given the relatively sparse number of observations and signal-to-noise issues at high latitudes.

Over land, we observe an inverse relationship between shorter ranges and spatially coherent variability (shorter $\langle a_{space} \rangle$ and higher $\langle c_s \rangle^{1/2}$ in the southeastern U.S. and western Canada). However, shorter $\langle a_{space} \rangle$ in high latitude ocean bins did not coincide with greater spatially coherent variability. Seasonal differences in $\langle a_{space} \rangle$ were all below 5 km when averaged by biome and insignificant compared to standard deviation of $\langle a_{space} \rangle$ within bins. The largest seasonal difference occurred over the midlatitudes, with $\langle a_{space} \rangle$ ~3-5 km greater on average during summer compared to winter. Our results suggest that systematic biases are present over all times of the year across the domain.

3.4.5 Random Fine-scale Variability in XCO_2

Random fine-scale variability $\langle c_0 \rangle^{1/2}$ in XCO_2 was 0.2 ppm on average for the full domain and ranged from 0.1 ppm to 0.4 ppm (Figure 6d). For all bins, $\langle c_0 \rangle^{1/2}$ was under 1 ppm, consistent with reported error from v10 OCO-2 ACOS data product. The boreal region had lower $\langle c_0 \rangle^{1/2}$ (0.27 ppm on average) compared to the continental temperate region which had the greatest $\langle c_0 \rangle^{1/2}$ (0.35 ppm on average) of all regions (Table 3). We note that the average for high latitude bins do not include winter months when there are gaps in data due to insufficient light. Over the ocean, $\langle c_0 \rangle^{1/2}$ was under 0.3 ppm and lower in high latitudes as well (Table 2). Compared to spatially coherent variability, $\langle c_s \rangle^{1/2}$, $\langle c_0 \rangle^{1/2}$ was a generally lesser portion of total fine-scale variability. Over the ocean, the fraction of random to total fine-scale variability decreases with latitude from ~30% in the subtropics to ~18% in high latitudes. We found a robust surface type dependence in $\langle c_0 \rangle^{1/2}$, which was typically twice as large when computed in soundings over land than ocean in mixed surface type coastal bins (0.1 ppm on average versus

0.3 ppm). Bins that have dominantly land surface type fractions tend to have twice as large $\langle c_0 \rangle^{1/2}$ compared to water bins, with the exception of some land bins in the high latitudes which have $\langle c_0 \rangle^{1/2}$ that is lower and more similar to the adjacent high latitude ocean. Our results suggest a land bias of ~0.1 – 0.2 ppm in random fine-scale XCO_2 variability, which is smaller in magnitude but more geographically robust than the potential land bias we observe in spatially coherent variability.

We observed very small seasonal differences in $\langle c_0 \rangle^{1/2}$ (below 0.1 ppm) over the ocean and greater seasonal differences over the continent (the majority of land bins had ~50% lower $\langle c_0 \rangle^{1/2}$ during the winter months compared to the average across all seasons). These results are consistent with Torres et al. (2019) who reported slightly lower random variability (0.5 ppm vs. 0.6 ppm) in 250-km high pass filtered v8 OCO-2 XCO_2 during winter months at Park Falls, WI and Lamont, OK. Despite low light/long path length conditions, $\langle c_0 \rangle^{1/2}$ was lower during the winter at higher latitudes of the domain, supported by Torres et al. (2019) findings that random variability near their northernmost TCCON site (Bialystok, Poland) was 0.2 ppm lower during the winter (they were only able to report an average for February) compared to summer months. The greatest seasonality occurred in bins over the southeastern U.S., where $\langle c_0 \rangle^{1/2}$ decreased by half (~0.2 ppm) from fall to winter. Averaged over the full continent, $\langle c_0 \rangle^{1/2}$ was greatest during summer and lowest during winter. In contrast, $\langle c_0 \rangle^{1/2}$ over the Great Lakes and following the Rockies was ~0.1 ppm greater during the winter compared to other seasons and relatively large compared to the rest of the continent. The seasonal differences we observe are on the order of reported posterior v10 L2 error estimates, which were only ~0.1 ppm over land (0.5 ppm in June vs. 0.6 ppm in December) and less than 0.1 ppm over the ocean (ranged from 0.39 ppm to 0.45

ppm, without a clear trend by season). Seasonality in $\langle c_0 \rangle^{1/2}$ may point to seasonally varying

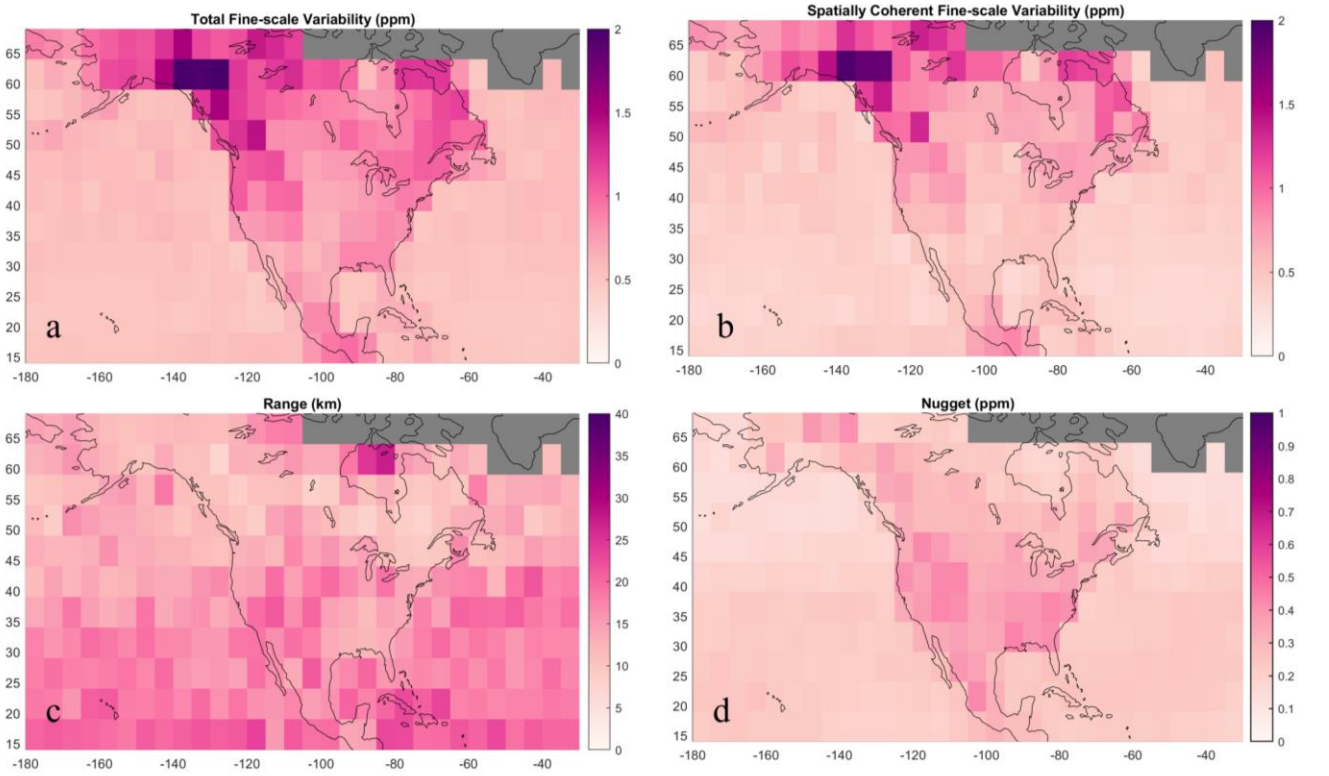sensitivity to cloud cover or surface heterogeneity, such as vegetation and ice.

Figure 6. Average characteristics of fine-scale (<250 km) variability. (a) total fine-scale

variability $\langle c_\infty \rangle^{1/2}$, (b) spatially coherent fine-scale variability, $\langle c_s \rangle^{1/2}$, the square root of the

difference between total variance and random variance $\langle c_\infty \rangle - \langle c_0 \rangle$, (c) geostatistical range

$\langle a_{space} \rangle$, the separation distance at which soundings become uncorrelated, and (d) random fine-

scale variability, $\langle c_0 \rangle^{1/2}$.

Table 4. Spatially-coherent fine-scale variability $\langle c_s \rangle^{1/2}$, random variability $\langle c_0 \rangle^{1/2}$, and

geostatistical range $\langle a_{space} \rangle$ by biome.

Region	$\langle c_s \rangle^{1/2}$ (ppm)	$\langle c_0 \rangle^{1/2}$ (ppm)	$\langle a_{space} \rangle$ (km)
N. A. Boreal	1.11	0.27	12
N Pacific Temperate	0.52	0.21	16
W Pacific Tropical	0.46	0.24	21
E Pacific Tropical	0.54	0.22	20
N.A. Temperate	0.76	0.35	15
Northern Ocean	0.67	0.17	14
N Atlantic Temperate	0.49	0.23	18
Atlantic Tropical	0.48	0.22	21
N Tropical S.A.	0.72	0.26	17
All	0.66	0.24	16

Table 5. Differences in average parameters of fine scale-variance computed using either nadir or glint observations for five bins in different continental zones.

Bin Location	Total variance $\langle c_s \rangle^{nadir} - \langle c_s \rangle^{glint}$ (ppm^2)	Spatially coherent Variance $\langle c_0 \rangle^{nadir} - \langle c_0 \rangle^{glint}$ (ppm^2)	Geostatistical range $\langle a_{space} \rangle^{nadir} - \langle a_{space} \rangle^{glint}$ (km)
Mexico 24-29° N 105-100° W	-0.08	0.01	-0.03
Eastern U.S. 34-39° N 85-80° W	-0.02	0.02	0.70

Western U.S. 39-44° N 120-115° W	0.01	0.02	-0.68
Eastern Canada 49-54° N 70-65° W	0.29	0.06	2.02
Western Canada 49-54° N 115-110° W	0.06	-0.02	-1.63

3.5 Relevance to Uncertainty Estimation in Inverse Modeling

Although most inverse model have a horizontal resolution sufficient to resolve synoptic scale variability, these models would still require estimates of the mean and error of fine-scale anomalies for each orbit with valid soundings in each model grid. One possible approximation of error would be to use standard error of the fine-scale anomalies for all soundings being averaged, N, assuming errors are independent for each sounding.

(8)

$$\sigma_{stderr} = \sqrt{\frac{\sigma_{finescale}^2}{N}} = \sqrt{\frac{\langle c_\infty \rangle}{N}}$$

Because of the large number of soundings, N, the standard error could be substantially underestimated if not all soundings are independent. We show that soundings are not all independent but instead correlated in groups within the separation distances estimated by geostatistical ranges. The observed ranges are much shorter than typical along-track averaging lengths used in inverse frameworks, such as across a 1x1 degree grid cell (~110 km) or the

length scale of 10 second averages (~70 km) (as in Crowell et al., 2019 and Peiro et al., 2022). To account for the spatial correlation of the soundings in the standard error estimate, one approach would be to include separate terms for random and spatially coherent variability. For the standard error of the spatially coherent variability, an effective degrees of freedom could be computed that better represents the independence of the data, N_{eff}. N_{eff} could be estimated using the along track averaging length, compared to the range. This assumes that each block of data equal to the size of the range is independent.

$$ (9) $$

$$ \sigma_{stderr} = \sqrt{\frac{\langle c_0 \rangle}{N} + \frac{\langle c_S \rangle}{N_{eff}}} $$

$$ (10) $$

$$ N_{eff} = \frac{\Delta x}{\langle a_{spatial} \rangle} $$

We compute standard error using both approaches (Eq. 8 and 9) for three averaging lengths of XCO$_2$; across a 5x5 degree box, a 1x1 degree box, and for a 10 second average (~70 km). In Figure 7a, we show the three different averaging lengths over which we compute fine-scale variability and spatial coherence for one orbit. Figure 7b shows the semivariogram and modeled c_∞, c_0, and $a_{spatial}$ computed over one orbit through a 5x5 degree box. The modeled parameter estimates computed over a 5x5 degree box were consistent with those computed on anomalies within the 1x1 degree box and the 10-second track length shown in Figure 7a. Model estimated $a_{spatial}$ was 20.6 km, c_∞ was 0.32 ppm^2 and c_0 was 0.06 ppm^2. Computed without incorporating fine-scale spatial coherence, σ_{stderr} was 0.03 ppm for the 5x5 degree aggregate,

0.04 for the 1x1 degree aggregate, and 0.05 ppm for the 10 second average. With spatial

coherence incorporated, σ_{stderr} was 0.14 ppm for the 5x5 degree aggregate, 0.22 ppm for the

1x1 degree aggregate, and 0.29 ppm for the 10 second average.

Using the average modeled fine-scale variance parameters for all 5x5 degree bins

(depicted in Figure 6), we compute an average σ_{stderr} for all 5x5 degree bins using both

approaches over the three averaging lengths. In Table 6, we present these results by biome.

When spatial coherence is not incorporated in the standard error calculation, σ_{stderr} is

underestimated on average by 0.22 ppm for 10 second aggregates, 0.14 for 1x1 degree

aggregates, and 0.07 for 5x5 degree aggregates. Standard error was largest for 10s aggregates in

the North American Boreal region (0.45 ppm) when incorporating geostatistical parameters into

the computation, significantly larger than standard error computed without geostatistical

parameters, 0.14 ppm (Table 5). All other regions in the domain had 10s aggregate standard error

between 0.2 and 0.4 ppm and were underestimated by ~0.2 ppm by the computation without

geostatistical parameters. For the other aggregation lengths, standard error (ranging from less

than 0.1 ppm to 0.3 ppm) was typically increased by 0.1 ppm when geostatistical parameters

were incorporated.

Figure 8 shows that σ_{stderr} exhibits a linear relationship with $\langle c_\infty \rangle$. For 10 second

aggregates, the linear slope is 0.36 with spatial coherence incorporated and 0.12 without.

Because bins with large $\langle c_\infty \rangle$ (>0.5 ppm) are shaped by large spatially coherent variability, $\langle c_s \rangle$,

rather than random variability, $\langle c_0 \rangle$, it is reasonable to assume their σ_{stderr} is increased by

correlated errors. Despite ocean bins having lower spatially coherent variability, indicating less

spatially coherent bias, σ_{stderr} is still typically underestimated by 0.1-0.2 ppm over the three

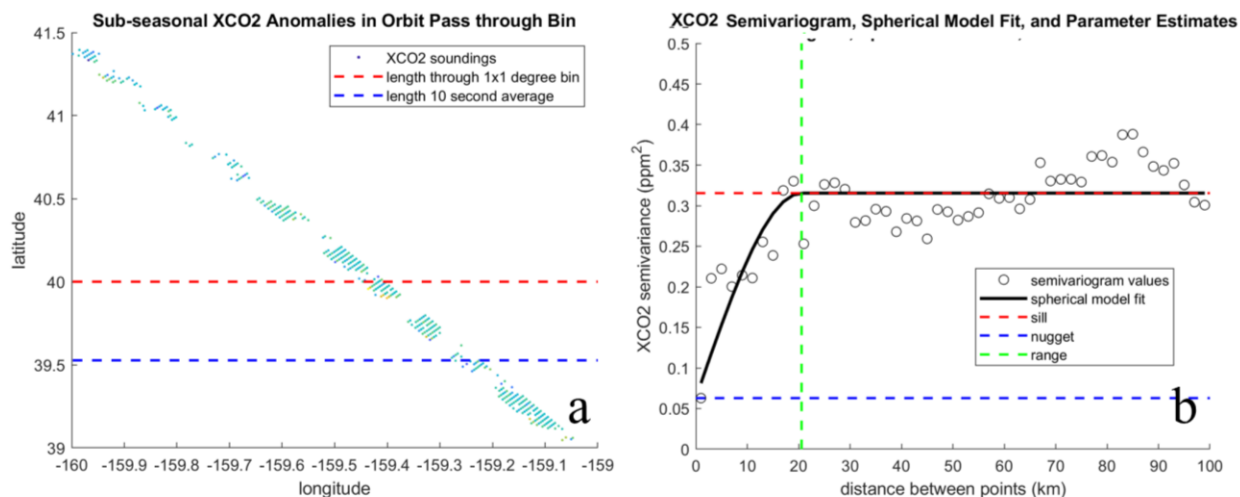averaging lengths, largely due to short geostatistical ranges.

Figure 7. For XCO$_2$ aggregated over one orbit through a 5x5 degree box, a 1x1 degree box, and over 10 seconds (a), 250km high pass filtered anomalies are fit with a semivariogram to estimate standard error (b). The experimental and modeled semivariogram, estimating total fine-scale variance c_∞, random variance c_0, and the geostatistical range a_{space}. Parameter estimates were consistent across all three averaging lengths.
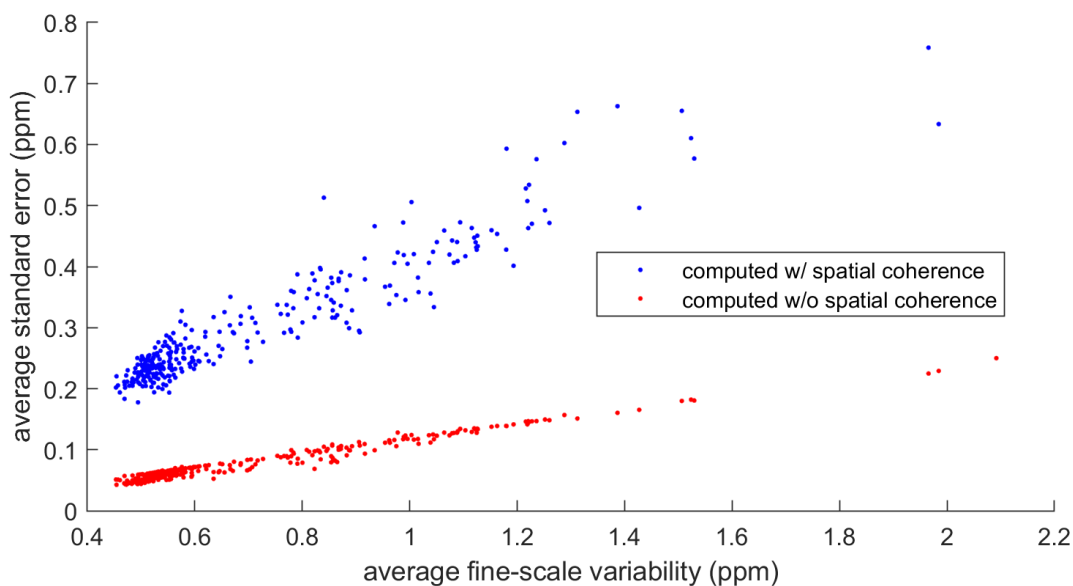
Figure 8. Comparison of average standard error σ_{stderr} computed for 70 km XCO_2 aggregates (corresponding to a typical 10-second average) for all orbit passes through 5x5 degree bins either with or without spatial coherence incorporated. Standard error scales with average fine-scale variability $\langle c_\infty \rangle$.

Table 6. Comparison of standard error in XCO_2 over typical averaging lengths (aggregated over 10 seconds, 1 degree latitude, and 5 degrees latitude) computed with or without spatial coherence by biome.

	σ_{stderr} 10s (ppm)	σ_{stderr} 10s (ppm)	σ_{stderr} 1°x1°(ppm)	σ_{stderr} 1°x1° (ppm)	σ_{stderr} 5°x5° (ppm)	σ_{stderr} 5°x5° (ppm)
N. A. Boreal	0.45	0.14	0.22	0.07	0.1	0.03
N Pacific Temperate	0.24	0.06	0.13	0.03	0.06	0.01
W Pacific Tropical	0.25	0.05	0.24	0.05	0.11	0.02
E Pacific Tropical	0.29	0.06	0.3	0.06	0.13	0.03
N.A. Temperate	0.35	0.09	0.25	0.06	0.11	0.03
Northern Ocean	0.3	0.08	0.17	0.05	0.08	0.02
N Atlantic Temperate	0.25	0.06	0.19	0.04	0.09	0.02
Atlantic Tropical	0.26	0.05	0.26	0.05	0.12	0.03
Tropical S.A.	0.35	0.09	0.38	0.1	0.17	0.04
All	0.30	0.08	0.19	0.05	0.09	0.02

4 Conclusions

We characterized the average seasonal cycle in OCO-2 v10 XCO_2 and partitioned sub-seasonal XCO_2 variability into synoptic and finer scales within 5x5 degree bins from 9-2014 to

12-2019 over North America and adjacent ocean basins. Using geostatistical analysis, we then quantified the magnitudes of spatially-coherent and random fine-scale (<250 km) along-track variability. Our results illustrate average variability on different scales and diagnose the relative influence of transport, patterns in surface fluxes, and error in the data. The primary motivation for our decomposition of variability was the present lack of understanding of fine-scale variations and correlations in XCO_2. Filtering out the main lower frequency modes of variability in XCO_2 (interannual, seasonal, and synoptic scales) uncovers local patterns in XCO_2 variability that are influenced by correlated error. While we uncovered new patterns in seasonal and synoptic-scale XCO_2 variability in this process, we will first discuss the implications of our fine-scale variability characterization as this is the least-resolved component of the XCO_2 variance budget and presents a large barrier in estimating inverted flux uncertainty.

Geostatistical parameters indicate where fine-scale (<250 km along-track distance) XCO_2 variability and correlations are driven by spatially-coherent biases. Over much of the continent, particularly in high latitudes, average spatially coherent fine-scale variability $\langle c_s \rangle^{1/2}$ reaches or exceeds 1 ppm. The large magnitude of $\langle c_s \rangle^{1/2}$ (computed as the mean from 9-2014 to 12-2019) cannot be reasonably explained by natural drivers like transport or local flux variability, which should produce spatially coherent variations on the order of 0.5 ppm or smaller over this short distance (Torres et al., 2019; Worden et al., 2017). In combination with length scales $\langle a_{space} \rangle$ shorter than that of mesoscale weather systems or spatial gradients driven by flux variability, we find that fine-scale XCO_2 over certain regions of the continent largely reflects correlated errors as opposed to real geophysical signals. Spatially coherent biases are larger over land ($\langle c_s \rangle^{1/2}$ was 0.9 ppm on average) than ocean ($\langle c_s \rangle^{1/2}$ was 0.5 ppm on average), but this relationship is not totally uniform. Correlated retrieval errors are widely known to be more prevalent over land,

where surface properties like albedo or topography are more variable. However, we find that spatial coherent biases also affect XCO_2 over the ocean, as shown by the short $\langle a_{space} \rangle$ values (17 km on average). Because ocean surface properties are less variable, correlated errors related to atmospheric parameters such as weather, clouds, or scatterers like aerosols may be driving the observed patterns. Errors over the ocean do not result in the large $\langle c_s \rangle^{1/2}$ as observed over land, but they do depress $\langle a_{space} \rangle$ and affect the independence of aggregated data.

Geostatistical analysis can improve estimates of XCO_2 aggregate uncertainty and help inform how different aggregation lengths cause correlated errors to have a greater or lesser effect on flux uncertainty. XCO_2XCO_2We recommend modeling groups increase aggregate uncertainty for aggregates with larger $\langle a_{space} \rangle$ and greater $\langle c_s \rangle^{1/2}$ by incorporating these metrics into their error computation as in Eqn. 9. In 10-second along-track XCO_2 aggregates (~70 km), standard error was underestimated on average by 0.22 ppm when geostatistical metrics were left out of the uncertainty computation. Standard error was also underestimated to a lesser degree in 1x1 degree aggregates (0.14 ppm greater on average using geostastical metrics) and in 5x5 degree aggregates (0.07 ppm greater). While the effect of correlated errors on aggregate uncertainty may be considered negligible for some of the domain, aggregates in bins that have very large $\langle c_s \rangle^{1/2}$ and long $\langle a_{space} \rangle$ such as over western Canada can be underestimated by a significant amount. The greatest underestimation of uncertainty occurred when using the shortest averaging length (10-s aggregates) in these bins; standard error increased by over 0.5 ppm on average when incorporating geostatistical parameters into the uncertainty computation. Correlated errors depress $\langle a_{space} \rangle$ to distances shorter than even the shortest averaging length typically used to assimilate the data and increase uncertainty the most in those 10-s aggregates. When comparing OCO-2 data with high-resolution simulations of XCO_2 such as CarbonTracker-Lagrange or WRF

forward model runs, $\langle a_{space} \rangle$ could be used to assess whether the spatial gradients in XCO₂ are valid (observations correlated at reasonable length scales versus too-short scales that reflect correlated errors).

We find distinct, coherent, geostatistical characteristics in XCO₂ over regions spanning over 1000s of kilometers. For example, $\langle c_s \rangle^{1/2}$ is consistently lower across the southeastern U.S. and greater over the continental tropics. Over the ocean, $\langle a_{space} \rangle$ tend to decrease with increasing latitude. This indicates semivariogram analysis does not necessarily have to be performed on each individual satellite overpass assimilated into inverse models. Computing semivariogram parameters can show what areas have related geostatistical characteristics due to either surface or atmospheric properties affecting the retrieval. Modelers could then choose representative areas to assign with unique fine-scale statistics and correlations to improve estimates of aggregate uncertainty in OCO-2 XCO₂ XCO₂for comparison with simulated XCO₂ in the model grid. Average geostatistical characteristics should also be computed by season; correlated errors produce features in $\langle c_s \rangle^{1/2}$ and $\langle a_{space} \rangle$ that emerge at different times of the year. Other features are present for most of the year, such as the great $\langle c_s \rangle^{1/2}$ over western Canada (we were only able to compute $\langle c_s \rangle^{1/2}$ during spring, summer, and fall, due to lacking winter observations in high latitudes). At minimum, geostatistical parameters should be computed to identify geographic locations like this with exceptionally large $\langle c_s \rangle^{1/2}$ and incorporate geostatistical metrics into error estimation.

The geostatistical parameters we computed show sharp, prominent land-ocean differences that emerge across coastlines. Inversion studies should consider how grid cells with both land and ocean surface types such as those over a coastline will represent two distinctly different XCO₂ distributions. In coastal bins, $\langle c_s \rangle^{1/2}$ could be up to twice as large when computed using

land versus water observations. Characterizing the different fine-scale statistics between XCO_2 retrieved over land and water is critical for regional emissions monitoring especially over coastal urban cities. These sharp contrasts do not emerge on scales that reflect real geophysical differences, as flux or transport variations create a smoother, larger spatial gradient in total column XCO_2. In the following paragraphs, we describe how real geophysical drivers create patterns in seasonal and synoptic-scale XCO_2.

The transport of large-scale flux patterns, rather than local flux seasonality, drives the seasonal cycle in OCO-2 XCO_2. The most pronounced spatial gradient in XCO_2 occurs during summer, with XCO_2-enriched air concentrated to the south of the jet stream and XCO_2-depleted air to the north caused by the hemispheric north-south distribution of biospheric carbon uptake. XCO_2 reaches a minimum during the fall, increases during the winter when biosphere respiration and fossil fuel emissions outweigh carbon uptake, and reaches a maximum in the spring with greatest XCO_2 to the north. This seasonally reversing gradient is acted on by mean zonal and synoptic-scale atmospheric circulation, driving the greatest variations in XCO_2 on seasonal and sub-seasonal scales. Average peak-to-trough seasonal cycle amplitudes in XCO_2 were between 4.5 ppm and 11.5 ppm and consistent with amplitudes over corresponding TCCON sites and estimated by model studies (Jacobs et al., 2021; Sweeney et al., 2015; Keppel-Aleks et al., 2012). Bins with negligible flux seasonality experience some of the greatest seasonal XCO_2 variability; the greatest amplitudes are concentrated in a band that extends from the Arctic to the mean path of the jet stream. Lower amplitudes are concentrated below this boundary and gradually decrease from north to south.

Seasonal XCO_2 amplitudes reflect the Northern Hemisphere north-south biospheric flux distribution and are spatially smoothed by large-scale atmospheric circulation, following mean

zonal flow and asymmetries. The otherwise smooth pattern in seasonal amplitudes arranged in east-west belts is disrupted over the western continent. A distinct land-ocean contrast manifests across the western coastline with seasonal amplitudes up to 2 ppm lower over the continent. Springtime detrended spatial means over the continent reach a lower maximum over the western continent that could result from dispersal of CO_2-enriched westerly air to the north and south of the coastline or a meridional transport pathway from lower latitudes up the western continent. This interesting feature prompts further scientific investigation to determine if the cause is not atmospheric circulation but instead a quasi-stationary systematic bias related to surface type, aerosols, or an interaction between retrieval variables.

Large-scale surface flux gradients are also responsible for XCO_2 variability on the synoptic-scale. Synoptic-scale advection of XCO_2 depleted air from higher latitudes and XCO_2 enriched air from southern latitudes during the summer produced average variability over 2 ppm. Because summertime synoptic variability is greater than other seasons due to differential north-south biologic uptake, its magnitude can be used for inferring trends in the strength of the biologic sink (Keppel-Aleks et al., 2012; Wunch et al., 2013). These variations are sufficiently large compared to background noise and fine-scale correlated errors in the midlatitudes to be captured by OCO-2 (1 – 2 ppm). While they are greater over the continent, they extend over the midlatitude Pacific and Atlantic ocean basins as well. Summertime synoptic variability correlates with the mean gradient in potential temperature at 700 hPa, indicating that dynamical tracers can be used to validate sub-seasonal variability in posterior XCO_2 fields produced by inverse models. Synoptic-scale XCO_2 variability was also significant outside the midlatitudes and summer months, over 0.5 ppm on average across the domain. Filtering out fine-scale variability, which

can be even larger than synoptic-scale variability at a given time and space, will help reveal the real flux and transport driven signals contained in synoptic-scale variability.

Our results show spatially-coherent retrieval biases still have a significant effect on the most recent version of XCO_2 (V10) over land and ocean biomes, despite great improvements in bias correction since previous versions of the data. Because each data version are known to be affected by correlated errors and each version of the algorithm is insensitive to correlations on small (<100 km) scales, the results of this study are relevant to previous and future versions of OCO-2 data. We observed the same feature of great $\langle c_s \rangle^{1/2}$ over British Columbia in v9 data. Future efforts to separate the influence of systematic errors from real variability would benefit from greater spatial coverage of in-situ or aircraft high resolution total column measurements, particularly near coastlines and the continental areas where we found greater $\langle c_s \rangle^{1/2}$. We suggest tracking changes in geostatistical parameters with each updated version of the retrieval algorithm changes in these key areas of interest. Though the challenge of attributing error-driven and real fine-scale variability in OCO-2 XCO_2 remains, our results show that geostatistical analysis can be used to diagnose biases, improve the representation of subgrid-scale XCO_2, and compute more accurate estimates of aggregate uncertainty in inverse modeling. With ongoing efforts to characterize the geostatistics of dense satellite observations like OCO-2 XCO_2 across multiple continents and ocean basins, researchers will be better equipped to link the growing wealth of data with surface measurements and model simulations, and will be able to more accurately constrain the unique spatial and temporal patterns of surface carbon flux regions.

Acknowledgments

Open Research.

The data produced in this study and used for this characterization of XCO_2 variability are available at the University of Virginia Dataverse, V1, "OCO-2 XCO_2 Seasonal and Sub-seasonal Variability Characterization (v10, 2014-2019)" via https://doi.org/10.18130/V3/GXOU0T (Mitchell, K., 2022). The retrieved Level 2 OCO-2 XCO_2 (version v10r) data used in this study are achived in NASA's Goddard Space Flight Center's Earth Sciences Data and Information Services Center (GES-DISC) permanent repository (http://disc.sci.gsfc.nasa.gov/OCO-2). MATLAB and Statistics Toolbox Release 2021a software used for this research is available via (https://www.mathworks.com/products/matlab.html) © 1994-2022 The MathWorks, Inc.

References

Baker, D. F., Bell, E., Davis, K. J., Campbell, J. F., Lin, B., & Dobler, J. (2022). A new exponentially decaying error correlation model for assimilating OCO-2 column-average CO2 data using a length scale computed from airborne lidar measurements. Geoscientific Model Development, 15(2), 649-668.

Baker, D. F., Bösch, H., Doney, S. C., O'Brien, D., & Schimel, D. S. (2010). Carbon source/sink information provided by column CO2; measurements from the Orbiting Carbon Observatory. Atmospheric Chemistry and Physics, 10(9), 4145–4165. https://doi.org/10.5194/acp-10-4145-2010

Baker, D. F., Law, R. M., Gurney, K. R., Rayner, P., Peylin, P., Denning, A. S., Bousquet, P., Bruhwiler, L., Chen, Y.-H., Ciais, P., Fung, I. Y., Heimann, M., John, J., Maki, T., Maksyutov, S., Masarie, K., Prather, M., Pak, B., Taguchi, S., & Zhu, Z. (2006). TransCom 3 inversion intercomparison: Impact of transport model errors on the interannual variability of regional CO 2 fluxes, 1988-2003. Global Biogeochemical Cycles, 20(1), n/a-n/a. https://doi.org/10.1029/2004GB002439

Basu, S., Baker, D. F., Chevallier, F., Patra, P. K., Liu, J., & Miller, J. B. (2018). The impact of transport model differences on CO2; surface flux estimates from OCO-2 retrievals of column average CO2; Atmospheric Chemistry and Physics, 18(10), 7189–7215. https://doi.org/10.5194/acp-18-7189-2018

Bell, E., O'Dell, C. W., Davis, K. J., Campbell, J., Browell, E., Scott Denning, A., ... & Weir, B. (2020). Evaluation of OCO-2 XCO_2 variability at local and synoptic scales using lidar and in situ observations from the ACT-America campaigns. Journal of Geophysical Research: Atmospheres, 125(10), e2019JD031400.

Byrne, B., Liu, J., Lee, M., & Bowman, K. W. (2021, December). Top-down North American CO_2 fluxes with a Nested Version of CMS-Flux. In AGU Fall Meeting Abstracts (Vol. 2021, pp. A12E-02).

Chevallier, F. (2007). Impact of correlated observation errors on inverted CO_2 surface fluxes from OCO measurements. Geophysical Research Letters, 34(24), L24804. https://doi.org/10.1029/2007GL030463

Corbin, K. D., Denning, A. S., Lu, L., Wang, J.-W., & Baker, I. T. (2008). Possible representation errors in inversions of satellite CO_2 retrievals. Journal of Geophysical Research, 113(D2), D02301. https://doi.org/10.1029/2007JD008716

Cressie, N., & Hawkins, D. M. (1980). Robust estimation of the variogram: I. Journal of the International Association for Mathematical Geology, 12(2), 115–125. https://doi.org/10.1007/BF01035243

Crisp, D., Pollock, H. R., Rosenberg, R., Chapsky, L., Lee, R. A., Oyafuso, F. A., ... & Wunch, D. (2017). The on-orbit performance of the Orbiting Carbon Observatory-2 (OCO-2) instrument and its radiometrically calibrated products. Atmospheric Measurement Techniques, 10(1), 59-81.

Crowell, S., Baker, D., Schuh, A., Basu, S., Jacobson, A. R., Chevallier, F., Liu, J., Deng, F., Feng, L., McKain, K., Chatterjee, A., Miller, J. B., Stephens, B. B., Eldering, A., Crisp, D., Schimel, D., Nassar, R., O'Dell, C. W., Oda, T., … Jones, D. B. A. (2019). The 2015–2016 carbon cycle as seen from OCO-2 and the global in situ network. Atmospheric Chemistry and Physics, 19(15), 9797–9831. https://doi.org/10.5194/acp-19-9797-2019

Dong, X., Yue, M., Jiang, Y., Hu, X. M., Ma, Q., Pu, J., & Zhou, G. (2021). Analysis of CO_2 spatio-temporal variations in China using a weather–biosphere online coupled model. Atmospheric Chemistry and Physics, 21(9), 7217-7233.

Eldering, A., O'Dell, C. W., Wennberg, P. O., Crisp, D., Gunson, M. R., Viatte, C., Avis, C., Braverman, A., Castano, R., Chang, A., Chapsky, L., Cheng, C., Connor, B., Dang, L., Doran, G., Fisher, B., Frankenberg, C., Fu, D., Granat, R., … Yoshimizu, J. (2017). The Orbiting Carbon Observatory-2: first 18 months of science data products. Atmospheric Measurement Techniques, 10(2), 549–563. https://doi.org/10.5194/amt-10-549-2017

Gaubert, B., Stephens, B. B., Basu, S., Chevallier, F., Deng, F., Kort, E. A., Patra, P. K., Peters, W., Rödenbeck, C., Saeki, T., Schimel, D., van der Laan-Luijkx, I., Wofsy, S., & Yin, Y. (2019). Global atmospheric CO2; inverse models converging on neutral tropical land exchange, but disagreeing on fossil fuel and atmospheric growth rate. Biogeosciences, 16(1), 117–134. https://doi.org/10.5194/bg-16-117-2019

Gurney, K. R., Law, R. M., Denning, A. S., Rayner, P. J., Baker, D., Bousquet, P., Bruhwiler, L., Chen, Y.-H., Ciais, P., Fan, S., Fung, I. Y., Gloor, M., Heimann, M., Higuchi, K., John, J., Maki, T., Maksyutov, S., Masarie, K., Peylin, P., … Yuen, C.-W. (2002). Towards robust regional estimates of CO2 sources and sinks using atmospheric transport models. Nature, 415(6872), 626–630. https://doi.org/10.1038/415626a

Hu, X. M., Crowell, S., Wang, Q., Zhang, Y., Davis, K. J., Xue, M., ... & DiGangi, J. P. (2020). Dynamical Downscaling of CO2 in 2016 over the contiguous United States using WRF-VPRM, a weather-biosphere-online-coupled model. Journal of Advances in Modeling Earth Systems, 12(4), e2019MS001875.

Jacobs, N., Simpson, W. R., Graham, K. A., Holmes, C., Hase, F., Blumenstock, T., ... & Warneke, T. (2021). Spatial distributions of XCO_2 seasonal cycle amplitude and phase over northern high-latitude regions. Atmospheric Chemistry and Physics, 21(22), 16661-16687.

Keppel-Aleks, G., Wennberg, P. O., & Schneider, T. (2011). Sources of variations in total column carbon dioxide. Atmospheric Chemistry and Physics, 11(8), 3581–3593. https://doi.org/10.5194/acp-11-3581-2011

Keppel-Aleks, G., Wennberg, P. O., Washenfelder, R. A., Wunch, D., Schneider, T., Toon, G. C., Andres, R. J., Blavier, J.-F., Connor, B., Davis, K. J., Desai, A. R., Messerschmidt, J., Notholt, J., Roehl, C. M., Sherlock, V., Stephens, B. B., Vay, S. A., & Wofsy, S. C. (2012). The imprint of surface fluxes and transport on variations in total column carbon dioxide. Biogeosciences, 9(3), 875–891. https://doi.org/10.5194/bg-9-875-2012

Kiel, M., O'Dell, C. W., Fisher, B., Eldering, A., Nassar, R., MacDonald, C. G., & Wennberg, P. O. (2019). How bias correction goes wrong: measurement of XCO_2; affected by erroneous surface pressure estimates. Atmospheric Measurement Techniques, 12(4), 2241–2259. https://doi.org/10.5194/amt-12-2241-2019

Kulawik, S. S., O'Dell, C., Nelson, R. R., & Taylor, T. E. (2019). Validation of OCO-2 error analysis using simulated retrievals. Atmospheric Measurement Techniques, 12(10), 5317–5334. https://doi.org/10.5194/amt-12-5317-2019

Lauvaux, T., Miles, N. L., Deng, A., Richardson, S. J., Cambaliza, M. O., Davis, K. J., Gaudet, B., Gurney, K. R., Huang, J., O'Keefe, D., Song, Y., Karion, A., Oda, T., Patarasuk, R., Razlivanov, I., Sarmiento, D., Shepson, P., Sweeney, C., Turnbull, J., & Wu, K. (2016). High-resolution atmospheric inversion of urban CO2 emissions during the dormant season of the Indianapolis Flux Experiment (INFLUX). Journal of Geophysical Research: Atmospheres, 121(10), 5213–5236. https://doi.org/10.1002/2015JD024473

MATLAB. (2021). version R2021a. Natick, Massachusetts: The MathWorks Inc.

Miller, C. E., Crisp, D., DeCola, P. L., Olsen, S. C., Randerson, J. T., Michalak, A. M., Alkhaled, A., Rayner, P., Jacob, D. J., Suntharalingam, P., Jones, D. B. A., Denning, A. S., Nicholls, M. E., Doney, S. C., Pawson, S., Boesch, H., Connor, B. J., Fung, I. Y., O'Brien, D., … Law, R. M. (2007). Precision requirements for space-based data. Journal of Geophysical Research: Atmospheres, 112(D10). https://doi.org/10.1029/2006JD007659

OCO-2 Science Team/ Gunson, M. R., , Eldering, A. (2020). OCO-2 Level 2 bias-corrected XCO_2 and other select fields from the full-physics retrieval aggregated as daily files, retrospective processing (Version 10r). [Data set] Goddard Earth Sciences Data and Information Services Center (GES DISC). doi: 10.5067/E4E140XDMPO2

O'Dell, C. W., Connor, B., Bösch, H., O'Brien, D., Frankenberg, C., Castano, R., ... & Wunch, D. (2012). The ACOS CO2 retrieval algorithm–Part 1: Description and validation against synthetic observations. Atmospheric Measurement Techniques, 5(1), 99-121.

O'Dell, C. W., Eldering, A., Wennberg, P. O., Crisp, D., Gunson, M. R., Fisher, B., Frankenberg, C., Kiel, M., Lindqvist, H., Mandrake, L., Merrelli, A., Natraj, V., Nelson, R. R., Osterman, G. B., Payne, V. H., Taylor, T. E., Wunch, D., Drouin, B. J., Oyafuso, F., … Velazco, V. A. (2018). Improved retrievals of carbon dioxide from Orbiting Carbon Observatory-2 with the version 8 ACOS algorithm. Atmospheric Measurement Techniques, 11(12), 6539–6576. https://doi.org/10.5194/amt-11-6539-2018

Olsen, S. C., & Randerson, J. T. (2004). Differences between surface and column atmospheric CO2 and implications for carbon cycle research. Journal of Geophysical Research, 109(D2), D02301. https://doi.org/10.1029/2003JD003968

Peiro, H., Crowell, S., Schuh, A., Baker, D. F., O'Dell, C., Jacobson, A. R., ... & Baker, I. (2022). Four years of global carbon cycle observed from the Orbiting Carbon Observatory 2

(OCO-2) version 9 and in situ data and comparison to OCO-2 version 7. Atmospheric Chemistry and Physics, 22(2), 1097-1130.

Rastogi, B., Miller, J. B., Trudeau, M., Andrews, A. E., Hu, L., Mountain, M., ... & Alden, C. B. (2021). Evaluating consistency between total column CO 2 retrievals from OCO-2 and the in situ network over North America: implications for carbon flux estimation. Atmospheric Chemistry and Physics, 21(18), 14385-14401.

Rayner, P. J., & O'Brien, D. M. (2001). The utility of remotely sensed CO 2 concentration data in surface source inversions. Geophysical Research Letters, 28(1), 175–178. https://doi.org/10.1029/2000GL011912

Sweeney, C., Karion, A., Wolter, S., Newberger, T., Guenther, D., Higgs, J. A., Andrews, A. E., Lang, P. M., Neff, D., Dlugokencky, E., Miller, J. B., Montzka, S. A., Miller, B. R., Masarie, K. A., Biraud, S. C., Novelli, P. C., Crotwell, M., Crotwell, A. M., Thoning, K., & Tans, P. P. (2015). Seasonal climatology of CO2 across North America from aircraft measurements in the NOAA/ESRL Global Greenhouse Gas Reference Network. Journal of Geophysical Research: Atmospheres, 120(10), 5155–5190. https://doi.org/10.1002/2014JD022591

Torres, A. D., Keppel-Aleks, G., Doney, S. C., Fendrock, M., Luis, K., de Mazière, M., Hase, F., Petri, C., Pollard, D. F., Roehl, C. M., Sussmann, R., Velazco, V. A., Warneke, T., & Wunch, D. (2019). A Geostatistical Framework for Quantifying the Imprint of Mesoscale Atmospheric Transport on Satellite Trace Gas Retrievals. Journal of Geophysical Research: Atmospheres, 124(17–18), 9773–9795. https://doi.org/10.1029/2018JD029933

Wesloh, D., Lauvaux, T., & Davis, K. J. (2020). Development of a Mesoscale Inversion System for Estimating Continental-Scale CO2 Fluxes. Journal of Advances in Modeling Earth Systems, 12(9). https://doi.org/10.1029/2019MS001818

Worden, J. R., Doran, G., Kulawik, S., Eldering, A., Crisp, D., Frankenberg, C., O'Dell, C., & Bowman, K. (2017). Evaluation and attribution of OCO-2 XCO_2 uncertainties. Atmospheric Measurement Techniques, 10(7), 2759–2771. https://doi.org/10.5194/amt-10-2759-2017

Wunch, D., Wennberg, P. O., Messerschmidt, J., Parazoo, N. C., Toon, G. C., Deutscher, N. M., ... & Notholt, J. (2013). The covariation of Northern Hemisphere summertime CO_2 with surface temperature in boreal regions. Atmospheric Chemistry and Physics, 13(18), 9447-9459.

Wunch, D., Wennberg, P. O., Osterman, G., Fisher, B., Naylor, B., Roehl, C. M., O'Dell, C., Mandrake, L., Viatte, C., Kiel, M., Griffith, D. W. T., Deutscher, N. M., Velazco, V. A., Notholt, J., Warneke, T., Petri, C., de Maziere, M., Sha, M. K., Sussmann, R., … Eldering, A. (2017). Comparisons of the Orbiting Carbon Observatory-2 (OCO-2) XCO_2 measurements with TCCON. Atmospheric Measurement Techniques, 10(6), 2209–2238. https://doi.org/10.5194/amt-10-2209-2017